THE PENNSYLVANIA STATE UNIVERSITY
SCHREYER HONORS COLLEGE

DEPARTMENT OF MECHANICAL ENGINEERING

Correlating Local and Global Tensile Deformation Behavior of AlSi10Mg Samples Fabricated Via Laser Powder Bed Fusion

CALEB FRONK
SPRING 2023

A thesis
submitted in partial fulfillment
of the requirements
for a baccalaureate degree
in Mechanical Engineering
with honors in Mechanical Engineering

Reviewed and approved* by the following:

Amrita Basak
Assistant Professor of Mechanical Engineering
Thesis Supervisor

Bo Cheng
Associate Professor of Mechanical Engineering
Honors Adviser

* Electronic approvals are on file.

ABSTRACT

AlSi10Mg, fabricated by the laser powder bed fusion (L-PBF) additive manufacturing process, offers many advantages compared to traditional cast material. In this study, its tensile properties are evaluated by investigating global and local deformation behavior via extensometer and strain gauge sensors. Samples are built using recycled AlSi10Mg powder on ProX-320 L-PBF equipment using vetted process parameters, as suggested by 3D Systems. The as-built samples contain a one-sided V-notch to precisely control the onset of failure. Strain gauges are installed near the notch region and the samples are tested on an MTS 50 kN electromechanical load frame.

The results show the L-PBF AlSi10Mg samples possess a large range of ultimate tensile and yield strengths. These mechanical performance inconsistencies highlight the need for appropriate and accurate monitoring systems for additively manufactured materials. In the elastic regime of each experiment, the strain recorded by strain gauge and extensometer increases both linearly and proportionally. Near failure, the strain gauge records higher strain in comparison to the extensometer due to its proximity to the notch tip. This deviation marks the beginning of plastic deformation. The strain gauge properly monitored and detected damage of the material prior to catastrophic failure. The experimental findings are also corroborated with finite element-based simulation results. In summary, this work establishes that strain gauge sensors can be used for online health monitoring of additively manufactured samples.

TABLE OF CONTENTS

LIST OF FIGURES iii

LIST OF TABLES vii

ACKNOWLEDGEMENTS viii

Chapter 1 Introduction 1

1.1 Motivation 2
1.2 Objectives 2

Chapter 2 Additional Background and Literature Review 4

2.1 Overview of Additive Manufacturing Processes 4
2.2 Overview of AlSi10Mg Produced by L-PBF 7
2.3 Characteristics of AlSi10Mg Processed by L-PBF 8
2.4 Early-Stage Damage Detection 11
2.4.1 Current State of Early-State Damage Detection for AM Materials 11
2.5 Overview of Strain Gauges 12
2.5.1 Use of Strain Gauges in Industry 13
2.5.2 Limitations of Strain Gauges 14

Chapter 3 Methods 16

3.1 Manufacturing of AlSi10Mg Samples 16
3.2 Strain Gauge Installation 18
3.3 Strain Gauge Data Collection 20
3.4 Tensile Testing Experimentation 22
3.5 Post-Processing 25
3.6 Stress-Strain Analysis 27
3.7 Finite Element Modeling: Via Abaqus 29

Chapter 4 Results and Discussion 32

4.1 Finite Element Modeling 32
4.2 Testing and Verification of Al6061-T6 35
4.2.2 Comparison of Strain Gauge and Extensometer Strain 37
4.3 Testing of L-PBF AlSi10Mg Samples 40
4.3.1 Unnotched Stress and Global Elongation Data 40
4.3.2 Notched Stress and Extensometer Strain Data 42
4.3.3 Comparison of Strain Gauge and Extensometer Strain 44
4.3.4 Strain Distribution Discussion 49

Chapter 5 Conclusion 52

5.1 Research Summary.....52
5.2 Limitations 53
5.3 Recommendation for Future Works.....54

LIST OF FIGURES

Figure 2.1: Schematic of Directed Energy Deposition (DED) Process. This figure is reproduced with permission from Elsevier [6].....5

Figure 2.2: Schematic of binder jetting process. This figure is reproduced with permission from Springer Nature [4]. 6

Figure 2.3: Schematic of Sheet Lamination AM Process This figure is reproduced with permission from Springer Nature [4]. 6

Figure 2.4: A schematic of L-PBF process. This figure is reproduced with permission from Elsevier [13]. 8

Figure 2.5: Stress-strain curves from vertical and horizontal build directions. This figure is reproduced with permission from Elsevier [14]. 10

Figure 2.6: Strain gauge diagram with common nomenclature. This figure is reproduced with permission from Springer Dordrecht [22]. 12

Figure 3.1: (a) Dimensions for AlSi10Mg sample (b) Build direction of AlSi10Mg sample [20]. This figure is reproduced with permission from TMS. 17

Figure 3.2: Strain Gauge Application Process. (a) As-built AlSi10Mg sample (b) Sample prepared for strain gauge adhesive via smoothing and cleaning (c) Strain gauge applied to sample (d) Soldered, fully prepared samples. 19

Figure 3.3: (From left to right) Samples 7-14, 7-7, 7-19 with strain gauges fully installed and ready for testing. 20

Figure 3.4: Schematic Diagram of Wheatstone Bridge Circuit. 21

Figure 3.5: Wheatstone Bridge circuit showing connection to DAQ and strain gauge. 21

Figure 3.6: Testing MATLAB Code to ensure signal input across strain gauge. 22

Figure 3.7: 50 kN load frame and accessory equipment at MRI.....23

Figure 3.8: Image of AlSi10Mg sample loaded through AVS software. Notice the digital points placed on the sample to track strain. 24

Figure 3.9: Processed strain data; before noise filtering and smoothing. 26

Figure 3.10: Comparison between raw, noisy data and both the averaging and Butterworth filtering methods 27

Figure 3.11: (A) Image showing definition of regions in Abaqus (B) Image showing boundary conditions applied (C) Mesh created for a representative sample.....30

Figure 4.1: Stress distributions at 10 kN across (A) the strain gauge region and (B) the extensometer region gathered via finite element simulations. 33

Figure 4.2: Strain distributions at 10 kN across (A) the strain gauge region and (B) the extensometer region gathered via finite element simulations. 33

Figure 4.3: Progression of strain throughout a tensile simulation. 34

Figure 4.4: Graph comparing percent elongation with stress across the unnotched, constant cross-section region of the Al6061-T6 samples. 35

Figure 4.5: Graph comparing stress across notch of a representative Al6061-T6 sample with strain calculated via extensometer. 37

Figure 4.6: Comparison of strain detected via strain gauge vs. extensometer for Al6061-T6 sample 1. 39

Figure 4.7: Global stress and elongation curve for constant cross-section AlSi10Mg samples. 41

Figure 4.8: Stress-strain curves for each AlSi10Mg sample. The stress is the max stress recorded across the notch. The strain is recorded via extensometer. 43

Figure 4.9: Stress-Strain curves for each L-PBF AlSi10Mg sample tested. 44

Figure 4.10: Comparison between strain recorded via extensometer and strain gauge sensor for Sample 7-4. 45

Figure 4.11: Comparison between strain recorded via extensometer and strain gauge sensor for Sample 7-6. 45

Figure 4.12: Comparison between strain recorded via extensometer and strain gauge sensor for Sample 7-7. 46

Figure 4.13: Comparison between strain recorded via extensometer and strain gauge sensor for Sample 7-11. 46

Figure 4.14: Comparison between strain recorded via extensometer and strain gauge sensor for Sample 7-14. 47

Figure 4.15: Comparison between strain recorded via extensometer and strain gauge sensor for Sample 7-19. 47

Figure 4.16: Stress-strain curves with strain gauge non-linearity point highlighted. One can see it nearly matches with the yield stress for each sample.....48

Figure 4.17: Strain gauge, extensometer, and global strain vs. time curves for ductile Al6061-T6 samples.....50

Figure 4.18: Comparison between strain gauge, extensometer, and global strain in each AlSi10Mg sample. The local strain never catches up to the percent elongation due to the lack of material ductility. 50

LIST OF TABLES

Table 3.1: AlSi10Mg sample ID and respective constant cross section dimensions 17

Table 3.2: AlSi10Mg sample ID and the respective notch-section dimensions.....18

Table 3.3: List of Boundary Conditions applied to Abaqus model.....30

Table 4.1: Summary of stress and strain distributions gathered via the finite element simulations shown in Figure 4.1 and 4.2 34

Table 4.2: Al6061-T6 Global Test Data. 36

Table 4.3: Al6061-T6 Extensometer Test Data 36

Table 4.4: Elastic Modulus of Al6061-T6 Samples Calculated Via Extensometer 37

Table 4.5: Summary of maximum loads and maximum stresses faced by AlSi10Mg samples in constant cross section portions. 41

Table 4.6: Summary of maximum stress (across notch) and strains 42

Table 4.7: End of linear matching portion - point where extensometer and SG strain deviate - for each AlSi10Mg sample 48

Table 4.8: List of maximum strain collected via strain gauge, extensometer, and elongation calculation. 49

Table 4.9: Percent increase from strain gauge strain to extensometer strain 51

ACKNOWLEDGEMENTS

The completion of my honors thesis marks a significant milestone in my journey towards graduating with an undergraduate degree in Mechanical Engineering. Two years ago, I became paired with my thesis supervisor Dr. Amrita Basak; the research helped give me greater interest and purpose within my degree.

I owe many thanks to Dr. Basak for her constant support. She always gave me freedom and perspective on what it means to do meaningful work and research. I owe thanks to the students in the Basak Lab, mainly Maxwell, Susheel, and Ritam, who I worked with along the way.

I will be forever grateful to Mr. Clyde Shuman for funding my research for these past two years. The Shuman scholarship enabled me to purchase supplies, become a user at the Materials Research Institute (MRI), and present at the 2023 TMS conference in San Diego, California. I am thankful for all those involved in the Shuman program, including Dr. Daniel Cortes and Lea Caprio; they helped me make the most of this incredible blessing.

I would like to thank my family–Mom, Dad, and Colby–for their endless support and love. I could not have accomplished anything without them. I am thankful for Penn State and the many friends and memories I made during my four years here. I am certainly proud to have called this place my home for the past four years. Finally, I thank God and praise him for providing me with endless blessings, and the strength and belief to chase my dreams.

Chapter 1

Introduction

Metal additive manufacturing (AM), also known as 3D printing, is an exciting area in the field of mechanical engineering. AM research surged in recent years because of its vast potential across a wide range of industries. When utilized appropriately, AM allows engineers several distinct advantages over traditional manufacturing. Because AM constructs parts via a layer-by-layer process, engineers can design parts with significantly more complex geometries with only a fraction of the waste [1]. In addition, traditional (subtractive) manufacturing requires significant infrastructure and is best suited for high-volume part production. Lead times are significantly lower when utilizing additive manufacturing. Therefore, it has the potential to thrive in industries, such as aerospace, where only one or a few parts are needed, and quick implementation of parts is crucial. Other examples of AM's design flexibility include the ability to combine several parts into one, the ability to incorporate complex internal passageways, and the ability to produce unique metal alloys for new applications [1].

While the benefits of AM are apparent, there are several drawbacks and unknowns surrounding its implementation into design. Specifically, parts produced via additive manufacturing have historically received issues with certification [1]. Governments and industries expect parts to be nearly exact every single time; some confusion exists to whether AM can achieve this. These inconsistencies appear in terms of not only shape, but also surface finish and mechanical properties [2]. Therefore, the engineering community facilitated major research towards optimizing a wide range of AM processes, materials, and monitoring systems.

1.1 Motivation

For any structural engineering application, mechanical properties lie at the forefront of material selection. Historically, additive materials display a large variation in tensile properties and possess microstructural inconsistencies that can negatively affect structural performance [3]. Many additive materials still require significant research before widespread structural utilization. Traditional materials, such as aluminum and titanium, are well understood by industry. Large databases quantify tensile strengths precisely enabling engineers to operate closer to factors of safety – increasing performance and while minimizing cost. The ultimate goal surrounding AM research is to ensure use of additive materials is as robust and confident as traditional materials.

This thesis focuses on one specific additive material: AlSi10Mg manufactured via laser powder bed fusion (L-PBF). Because of its high strength to weight ratio, this form of additive aluminum is a prime contender for structural use in both the aerospace and automotive industries. Ultimately, this research aims to increase the understanding of the material's mechanical properties and compatibility with strain gauge sensors. The final goal focuses on the mechanical behavior of the L-PBF processed AlSi10Mg.

1.2 Objectives

This research has several thrusts which enable a thorough understanding regarding the mechanical behavior of the material. First, the research aims to run successful tensile testing on AlSi10Mg – additively manufactured aluminum – samples and collect accurate global stress and elongation data. This global data is helpful for understanding the overall mechanics of the material.

In addition to global data collection, strain gauges and a virtual extensometer will pinpoint local strain highlighted around a notch region. Strain gauges are installed in closer proximity to the notch tip. The local strain data will then be compared to global data to highlight the differences between the two.

The entirety of the local and global strain data will be important for developing complete stress-strain data for AlSi10Mg. These results–such as the strain distributions—will be corroborated via Abaqus finite element simulations.

Another research thrust revolves around the use of strain gauges on additively manufactured materials. Relatively, few studies exist that couple AM materials and strain gauges for early-stage damage detection. This research attempts to prove strain gauges can be successfully applied to additive materials and used for early-stage damage detection.

Chapter 2

Additional Background and Literature Review

This chapter presents additional background and literature relevant to the thesis. First, the chapter presents the four major additive manufacturing techniques and processes. After this section, the literature review focuses on one specific additive material: AlSi10Mg produced via Laser Powder Bed Fusion (L-PBF). This section highlights the important material characteristics and transitions into the need for early-stage damage detection methods. Lastly, the literature review presents an overview of strain gauges in industry and additive manufacturing. Ultimately, this section aims to give sufficient background to the topic, while demonstrating exactly where this experimentation is novel to the research community.

2.1 Overview of Additive Manufacturing Processes

There are four main metal additive manufacturing processes discussed in this literature review: directed energy deposition (DED), binder jetting, sheet lamination, and powder bed fusion (PBF) [4]. These methods primarily vary by their feedstocks (powder, wire, or sheet metal), feedstock delivery mechanisms, and bonding techniques. As a result, each method possesses costs and benefits associated with a part's desired application.

Powder bed fusion is one method commonly used in AM. The PBF method rolls a layer of powder onto a build platform and employs a high energy device—commonly a laser—to sinter select areas based on an uploaded computer-aided design file [5]. Once a given layer is sintered (and/or melted), the build platform is lowered enabling the process to continue until a full part is constructed. Other nicknames for PBF include selective laser sintering, selective laser melting, and electron beam melting—although these processes have slight variation.

Directed energy deposition, shown in Figure 2.1, utilizes a highly energized heat source, such as a laser, and nozzle to lay down either powder or wire feedstock locally and melt it into the part [6]. DED is similar to the powder bed fusion process but deviates in its material deposition method. During the transition from one layer to the next, DED moves the delivery nozzle, while powder bed fusion moves the build platform. Neither process is necessarily superior in comparison; preference depends on application. For example, DED is advantageous for manufacturing larger parts. DED allows for utilization of a variety of feedstock. It enables control for localizing part characteristics [6].

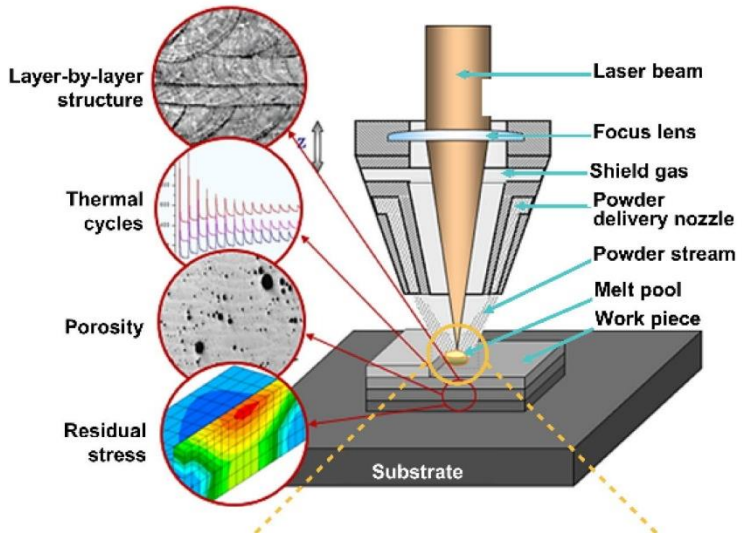

Figure 2.1: Schematic of Directed Energy Deposition (DED) Process. This figure is reproduced with permission from Elsevier [6].

Binder jetting, like the PBF processes, lays down a powder layer across the build platform [7]. However, the process is unique because of its two-stage binding process. In the first stage, a nozzle applies a liquid binder (essentially a glue) to select areas of the powder, forming a layer of the part. The build platform is then lowered, a new powder bed is laid, and the binder is applied. This process is illustrated in Figure 2.2. In the next stage, which consists of post-processing, the part is “debinded” through heat treatment and sintering. The post-processing stage helps fully bond particles together and

produce a higher part density. The binder jetting process can utilize a plethora of materials and avoids the need for the inert environments needed for DED or PBF.

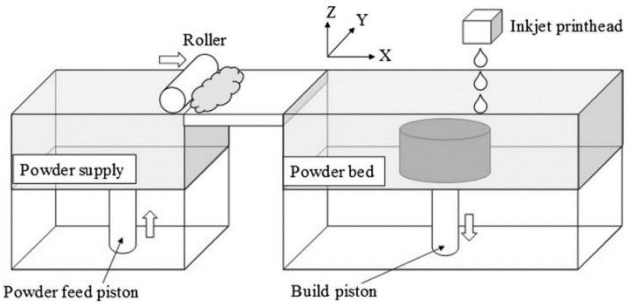

Figure 2.2: Schematic of binder jetting process. This figure is reproduced with permission from Springer Nature [4].

The last of the four main AM methods is sheet lamination. This process, also known as laminated object manufacturing, employs a high energy source to bond layers of metallic sheet metal together [4]. After bonding the sheet layers together, a tool cuts the part to shape, and the process repeats. The most common method for sheet lamination utilizes a device called a sonotrode to emit ultrasonic waves and create a mechanical pressure that bonds the sheet layers together. This method helps avoid residual stresses formed by repetitive heating. A schematic diagram of sheet lamination through ultrasonic consolidation is shown in Figure 2.3.

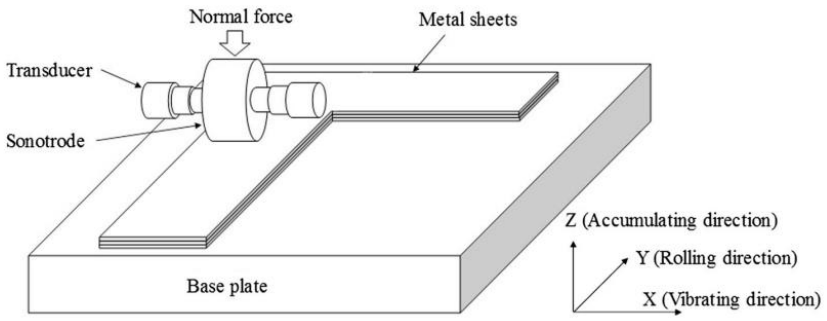

Figure 2.3: Schematic of Sheet Lamination AM Process This figure is reproduced with permission from Springer Nature [4].

2.2 Overview of AlSi10Mg Produced by L-PBF

Based on the plethora of metal AM techniques, selecting a specific one may seem overwhelming. Non-technical selection factors include cost, print time, and part size. From a technical side, material compatibility is one of the most significant factors in method selection [8]. Parts produced by each AM method experience different heating and cooling rates. For example, L-PBF and electron powder bed fusion (E-PBF) are both considered powder bed fusion processes but possess significantly different cooling rates. A brittle material may crack due to the fast cooling of laser powder bed fusion. On the other hand, due to the high temperature bed (greater than 870 Kelvin), a material with a low melting point could not be produced E-PBF.

Laser powder bed fusion (L-PBF), shown in Figure 2.4, employs a laser beam as the high energy source that sinters select areas of the of the powder bed. L-PBF is commonly chosen due to its fast-cooling rates which encourages the development of fine microstructures. AlSi10Mg, an aluminum alloy with near eutectic (homogenous) composition, is a common choice for L-PBF processes [9],[10]. Due to favorable mechanical properties and weldability, Aluminum-Silicon alloys are of particular interest for both AM and non-AM applications [11]. Al-Si alloys, such as AlSi10Mg, are commonly fabricated by casting. However, they are also processed using AM. AlSi10Mg can withstand the rapid solidification that causes cracking in many other additively manufactured metals. In fact, the fine microstructure of L-PBF AlSi10Mg gives it superior mechanical properties, such as higher tensile strength and hardness, compared to its cast counterparts [12]. Like other aluminum alloys, AlSi10Mg provides a high strength to weight ratio, which makes it an ideal candidate for integration in the aerospace industry.

Research focusing on AM AlSi10Mg follows two main tracks. The first focuses on optimizing process parameters during manufacturing, and the second focuses on the corresponding mechanical properties. Many researchers found that AlSi10Mg has a wide range of tensile properties. Therefore, it is important to understand how underlying microstructure relates to this variation.

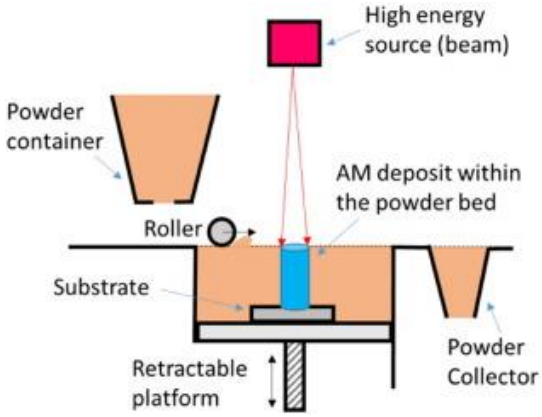

Figure 2.4: A schematic of L-PBF process. This figure is reproduced with permission from Elsevier [13].

2.3 Characteristics of AlSi10Mg Processed by L-PBF

Historically, parts produced by additive manufacturing show anisotropic and heterogeneous mechanical properties [13]. Anisotropy occurs when the mechanical response of a material varies with the loading direction. Heterogeneity refers to inconsistent microstructure or mechanical properties throughout a specimen. Many researchers have attributed this heterogeneity to the complex and repeated thermal cycles that AM parts undergo during processing. Meanwhile, build direction and orientation are viewed as the leading causes for anisotropy. Previous research around AlSi10Mg also shows a variation of mechanical properties that will be explored in this next section.

Hyer *et al.* [4] studied the different microstructural characteristics of AlSi10Mg produced by L-PBF after altering different processing parameters. These parameters include laser power, hatch spacing, scan speed, slice thickness, and the normalized energy density. Unlike previous studies, they were varied to extreme magnitudes. Analysis of the microstructure revealed an inconsistent cell structure around the melt pool (area where the laser bonds the layers). Grains near the melt pool boundary appeared coarser compared to smaller sized grains within the melt pool, which pointed towards the boundary's center.

In addition to differences around the melt pools, the L-PBF processes have been hypothesized to form a different microstructure in the top of the specimen compared to the bottom. Hadadzadeh *et al.* [3]

investigated the effects of repeated thermal cycles on AlSi10Mg samples. It was determined that slight variation existed between the top and bottom of the print, mainly characterized by the formation of different precipitates due to different cooling rates. However, hardness testing performed on different areas of the specimen found no significant variation of mechanical properties. It is important to note that hardness testing shows inconsistencies for deriving tensile properties.

Paul M *et al.* [14] sought to explore the reason behind the anisotropy of L-PBF AlSi10Mg with regards to fracture toughness and stress-strain data. Tensile testing was performed on samples manufactured in two different build directions: vertical and horizontal. These samples showed different orientations of heat-affected zones, and therefore different fracture mechanisms. The samples built in the vertical direction showed slightly greater strength, but lower ductility compared to the horizontally built samples. Results from this study, including visual definitions of build directions, can be seen in Figure 2.5. Similar results were found by AlRedha *et al.* [15]. When studying AlSi10Mg made by L-PBF, they determined that the material, depending on orientation, promotes different slip mechanisms. Slip, and the resulting fracture, either follows grain boundary paths, or breaks through them. This provides an explanation for material anisotropy. Again, simple tensile testing revealed horizontally built samples showed greater ductility than vertically built ones.

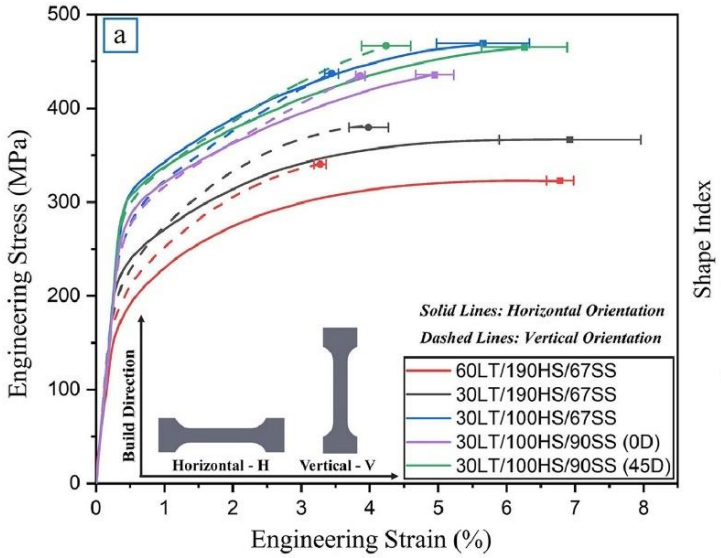

Figure 2.5: Stress-strain curves from vertical and horizontal build directions. This figure is reproduced with permission from Elsevier [14].

One interesting investigation of AlSi10Mg also found that fracture mechanisms vary upon loading direction [16]. The horizontally built specimen has cracks propagate across melt pool borders while vertically built specimens have cracks travel along the melt pool border. The study concludes that although strain localization exists along melt pool boundaries, no macroscopic strain localization exists. Zhoa L *et al.* [16] deviates from previous literature on the topic of mechanical properties and states that the material is nearly isotropic. While the article emphasizes this conclusion, it attaches to it many stipulations. The study explains that when examining true strain, the elongation at fracture for both loading directions is the same. It explains the importance of having ideal manufacturing conditions for nearly isotropic results. At this moment, there are too many manufacturing inconsistencies to universally apply this conclusion. However, the article facilitates a new conversation about this heavily researched material.

In summary, because AlSi10Mg is manufactured (and sintered) layer by layer, the greatest weaknesses lie within the heat affected zone between layers, where also the melt pool border exists. If a specimen is loaded perpendicular to the melt pool borders, cracks propagate along the borders.

Meanwhile, if loaded parallel to the melt pool borders, cracks break across each melt pool boundary. Therefore, AlSi10Mg is considered anisotropic and often heterogeneous.

2.4 Early-Stage Damage Detection

While creating safe design is a first requirement for engineers, it is essential to properly monitor structural components throughout their life cycles. Therefore, the field of early-stage damage detection is critical for understanding real-time loading conditions of a structure and avoiding catastrophic failure [17]. It also gives engineers a tool to assess the need for preventative maintenance or retirement of equipment. Damage detection spans many industries and incorporates an assortment of sensor technologies and data analysis methods. It includes both quantitative and qualitative techniques. Qualitative methods focus on the identification of cracks from visual tests. Quantitative methods include, but are not limited to, ultrasonics, acoustics, eddy currents, and strain gauges.

2.4.1 Current State of Early-State Damage Detection for AM Materials

Due to the previously highlighted consistency, heterogeneity, and anisotropy issues of additively manufactured parts, having strong monitoring systems for AM parts is especially pertinent. Reliable detection systems allow for more confident use of AM and can expedite the use of parts in industry. Therefore, many researchers are focused on proving that AM parts are compatible with sensor technology. Several examples are presented in this research.

One commonly used method for damage detection is through wave propagation methods. Piezoelectric transducers send and receive ultrasonic waves into the material being tested. If the wave interacts with any sort of discontinuity, such as a crack, the signal will be distorted [18]. Modir *et al.* [19] employed piezoelectric elements to monitor health of AM samples with different infill densities. The

research method (named the SuRE method) was successful in monitoring compressive forces applied to the AM samples. Another example of a research study focused on evaluating the condition of AlSi10Mg. Dharmadhikari *et al.* [20] focused a confocal microscope on the root of the notch to observe the development of cracking and calibrate the force-time data from the force sensors. The paper uses two different methods for early fatigue detection, one based on energy dissipation and the other based on reduction in stiffness. Both methods were successful but may be costly to implement in industry.

2.5 Overview of Strain Gauges

A strain gauge is a type of sensor commonly used in the field of engineering to detect strain (the percent change in length). During an event that produces deformation, the strain gauge, and its respective wiring elongate, changing the resistance of the gauge [21]. This alters the corresponding voltage through a circuit, measured by a data acquisition device. Commonly, a Wheatstone bridge circuit is used to monitor these changes. The change in voltage can be plugged into an equation to determine percent strain. Figure 2.6 shows a diagram of a strain gauge and common terms used to describe the layout.

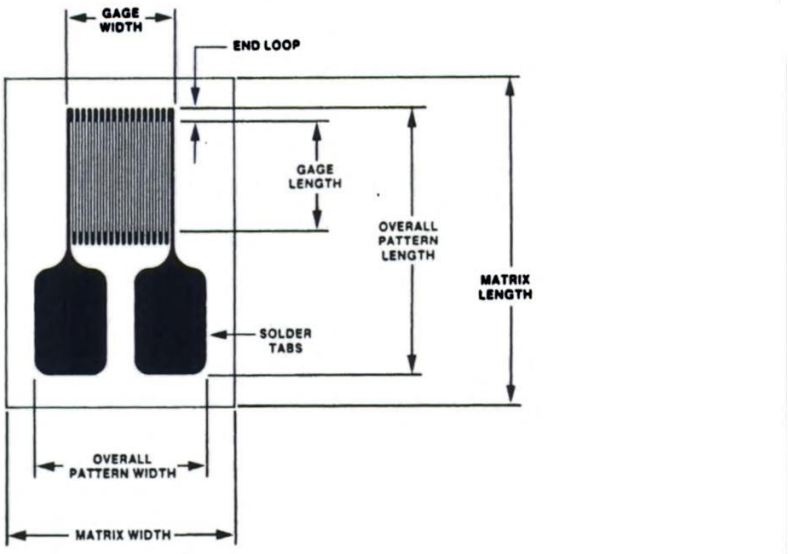

Figure 2.6: Strain gauge diagram with common nomenclature. This figure is reproduced with permission from Springer Dordrecht [22].

The application of strain gauges for early damage detection offers several benefits. The first benefit revolves around their relatively tiny size. Strain gauge sizes are often on a scale of millimeters, which allows them to be placed on many different surfaces and in a variety of applications. These applications range from medical devices to aerospace technologies such as turbine blades. Application even exists within the construction industry. Second, strain gauges are comparatively cheaper than other monitoring technologies. Acoustic emission sensors and ultrasonic transducers cost thousands of dollars to purchase and install. Microscopes and imaging technologies can add up to over $100,000. Meanwhile, a high-quality strain gauge will cost around $100, with an additional cost to purchase the materials required for installation. Cheap, poor-quality gauges for experimental purposes can be purchased for less than $10. Along with their relatively cheap cost, strain gauges can be relatively simple to install. It may only take a few training sessions for a non-professional to learn the installation procedure.

Strain gauges are additionally beneficial because they allow for continuous monitoring of strain. Other health monitoring techniques and technologies, such as eddy current testing, require the machinery or equipment to be stopped and checked as a part of maintenance. Visual inspection of gas turbine technology cannot be performed during operation, and inspection after each use may be time consuming and unreliable. Strain gauges are different; they give real-time, during operation data.

2.5.1 Use of Strain Gauges in Industry

Engineers and researchers employ strain gauges for many different purposes. Identifying localized strain [23], modeling [24], and testing [25] all encompass suitable applications. In this next section, the versatility of strain gauges will be shown with several examples.

Rumsey *et al.* installed strain gauges on the blades of a wind turbine and conducted fatigue testing [26]. Strain gauges monitored the health of the blades. The strain gauge data tracked a slight

reduction in stiffness of the carbon fiber, showing that the damage was properly monitored by the gauge. In a different application, Rawal *et al.* used strain gauges as a precursor to fatigue testing [25]. Researchers wanted to conduct fatigue testing on a bracket composed of the additively manufactured titanium alloy (Ti-6AI-4V). The strain gauges recorded a range of 8000 micro strains, which was used as a parameter for fatigue testing. This study helps to show some of the compatibility of strain gauges with AM.

Strain gauges can also be used to gather local strain information for modeling and assessment purposes. In one example, strain gauges were used to model the bending moments of a propeller shaft in a ship [24]. As a result of disproportionate damage to a particular bearing, researchers wanted to determine optimal bearing placement along the shaft. They presented an updated, data driven approach to shaft bearing placement design. It proved effective in reducing bearing damage. Perbawa *et al.* [23] conducted axial compression tests on rock samples. He explored the difference between the global strain shown in cap-to-cap measurements (which can magnify biases), and localized strain determined through the application of strain gauges. The strain gauge data was insightful and showed no incorporation of bending. This experiment showed that strain gauges are valuable for comparing local and global strain. The study overcame the rock's poor surface finish to install the strain gauges.

2.5.2 Limitations of Strain Gauges

Several important considerations with regards to the limitations of strain gauges should be accounted for before conducting experimentation. The first limitation occurs in terms of the installation process. Strain gauges are bonded to the sample via glue or adhesive. Therefore, it is important for the specimen to have a smooth surface finish prior to installation. Some literature proves that strain gauges can still be applied to rough materials, but surface processing must occur [23]. Another important factor comes in terms of soldering. A frequent mistake includes improperly soldering the lead wires to the gauge

tabs [27]. Inexperienced personnel could potentially send too much heat to the foil, altering the sensitive layout. In addition, uniaxial strain gauges need to be aligned with the loading direction, or else they will record incorrect data. Lastly, it is important to understand that these sensors are applied to the surface of a part; therefore, resulting strain can only be interpreted as localized surface strain.

Another important consideration involves strain gauge failure. One article interprets strain gauge data and models it for two main failure types: debonding and loose lead termination [28]. When employing strain gauges for structural health monitoring purposes, there needs to be a distinction between compromised health of the sensor and the actual structure. Debonding occurs when the strain gauge no longer sticks to the surface of the sample. Loose-lead termination occurs when a wire disconnects from the strain gauge tab, losing signal to the processing unit. These errors must be considered during strain gauge experimentation. Fortunately, some researchers helped address the debonding scenario. Dos Reis *et al.* [29] conducted an experiment and produced a method very sensitive to debonding, based off measuring the temperature of the strain gauge grid. Proper attention to detail and use of proper data methods can help users mitigate some of these limitations.

Chapter 3

Methods

3.1 Manufacturing of AlSi10Mg Samples

The samples used in the study are made from two different materials: Al6061-T6 and additively manufactured AlSi10Mg. Al6061-T6, commonly used in aerospace applications, boasts an ultimate tensile strength of 310 MPa, a yield strength of 276 MPa, and a fatigue strength and fracture toughness of 96.5 MPa and 29 MPa-$m^{1/2}$ respectively [30]. The material is particularly advantageous because of its high strength to weight ratio. The design of the samples, following the ASTM E466 standard [31] are shown in Figure 3.1(a). Al6061-T6 sheets of thickness 2.29 mm are acquired from McMaster-Carr and the samples are extracted from the sheets using waterjet machining. The notch geometry used in the designs is intended to induce a high stress concentration. The study utilizes the standard A6061-T6 as a baseline for comparison to the additive aluminum.

The additively manufactured AlSi10Mg is manufactured via laser powder bed fusion (outlined in Chapter 2) and recycled powder. 3D systems – a 3D printing company based in Rock Hill, South Carolina, USA – provided the powder used to manufacture the samples in the study. As obtained via energy dispersive x-ray spectroscopy (EDS), the composition of the powder is as follows: 86.83 wt. % Al, 11.83 wt. % Si, 0.34 wt. % Mg, 0.96 wt. % O, and 0.04 wt. % Fe. The samples used in this study are manufactured on a ProX-320 laser powder bed fusion (L-PBF) equipment. Penn State's Center for Innovative Materials Processing through Direct Digital Deposition (CIMP-3D) utilized the following vetted process parameters: layer thickness of 60 μm, laser power of 325 W, and scanning speed of 1400 mm/s. A striped hatch design pattern with hatch spacing 82 μm is used [20]. These samples in this study were tested in as-built condition without any post-processing. Like the Al6061-T6 samples, v-notched

samples are used in the study. An image of the sample dimensions can be seen in Figure 3.1. The samples were built in the horizontal build direction, which can also be seen in Figure 3.1.

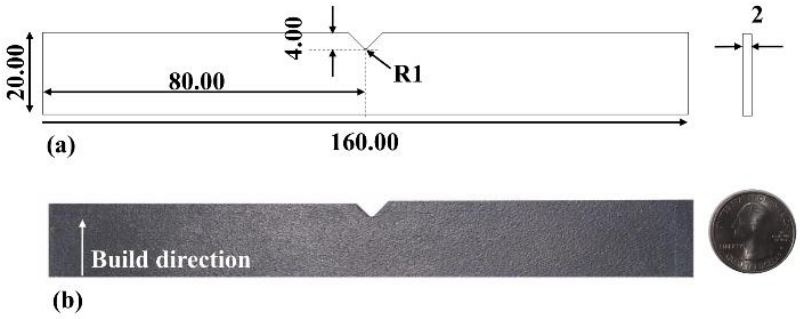

Figure 3.1: (a) Dimensions for AlSi10Mg sample (b) Build direction of AlSi10Mg sample [20]. This figure is reproduced with permission from TMS.

It is important to note that there was slight deviation in the dimensions of each AlSi10Mg sample. For completeness, calipers were used to gather the dimensions for each sample. These complete dimensions are shown in Tables 3.1 and 3.2 below. These dimensions are important for later deriving stress calculations.

Table 3.1: AlSi10Mg sample ID and respective constant cross section dimensions

Sample ID	Thickness (mm)	Width (mm)	Cross Sectional Area (mm^2)	Gauge Length (mm)
7-4	2.17	19.66	42.66	89.5
7-6	2.14	19.70	42.16	91.2
7-7	2.05	19.78	40.55	91.0
7-11	2.09	19.70	41.17	88.5
7-14	2.06	19.77	40.73	94.0
7-19	2.01	19.80	39.80	94.0

Table 3.2: AlSi10Mg sample ID and the respective notch-section dimensions

Sample ID	Thickness (mm)	Notch width (mm)	Cross Sectional Area (across notch) (mm^2)
7-4	2.17	15.66	33.98
7-6	2.14	15.70	33.60
7-7	2.05	15.78	32.35
7-11	2.09	15.70	32.81
7-14	2.06	15.77	32.49
7-19	2.01	15.80	31.76

3.2 Strain Gauge Installation

In preparation for the mechanical testing, strain gauges are applied to the samples near the notch. Strain gauge installation follows a three-step process: sample preparation, strain gauge attachment, and soldering. Before attaching a strain gauge, the surface requires both smoothing and cleaning. The poor surface finish of the AM sample makes this process slightly more intensive. It is much more straightforward to attach a strain gauge to the smooth Al6061-T6 samples. The AlSi10Mg sample is sanded with both coarse and fine grit papers to achieve a smooth finish. Water is used to wash away debris and dust after each sanding turn. MCA-1 M-Prep Conditioner (mild phosphoric-acid) and MN5A-2 M-Prep Neutralizer (ammonia-based liquid) from VPG sensors are used in combination to achieve a clean surface. The use of the phosphoric acid allows for an accelerated surface cleaning process [33]. A clean surface, ready for adhesive use, is shown in Figure 3.2(b).

During the bonding stage, an M-Bond 200 Catalyst and Adhesive pairing from VPG are utilized. Using tweezers to avoid finger oil contamination on the sample, the strain gauge is placed near the notch in the desired application area. Gauge application tape allows the gage to be temporarily removed, so that

one can swiftly apply the adhesive and then press the strain gauge into place. The pair is allowed to cure for 1 day, sticking the ED-DY-125AD-350 strain gauge to the sample, as shown in Figure 3.2(c).

The last step involves soldering lead wires to the strain gauge tabs. One must exercise care when soldering to avoid damage to the strain gauge foil. After the attachment of the lead wires to the strain gauge tabs, M-Line Rosin Solvent is applied to the installation area. The solvent removes rosin flux residues, providing a cleaner signal to the acquisition device. Finally, M-Coat A Air Drying Polyurethane Coating is applied to the gauge. This coating takes roughly 2 hours to completely dry and gives protection against damage in a laboratory setting. Figure 3.2 illustrates the complete strain gauge application process from start to finish. Figure 3.3 shows several strain gauges attached to AlSi10Mg samples ready for testing.

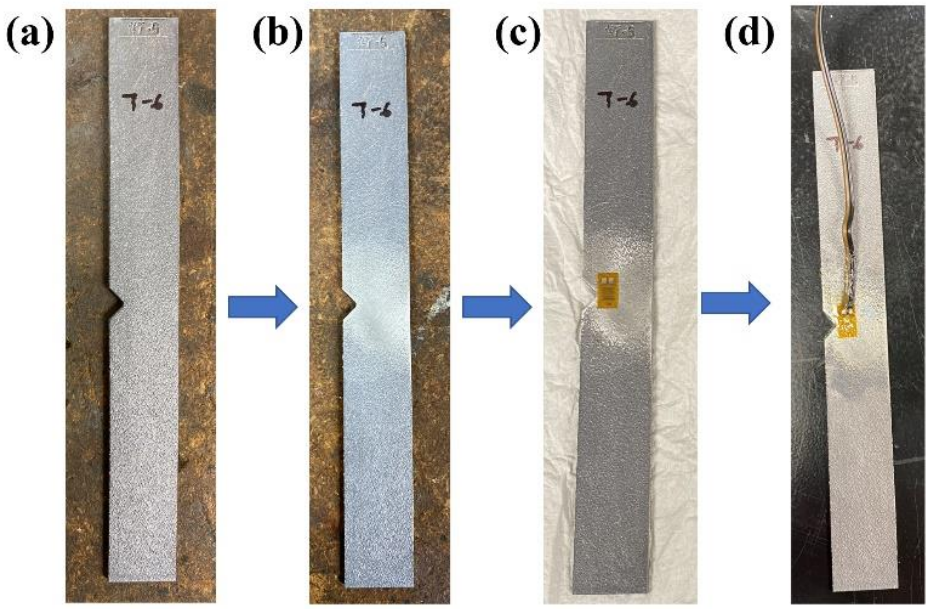

Figure 3.2: Strain Gauge Application Process. (a) As-built AlSi10Mg sample (b) Sample prepared for strain gauge adhesive via smoothing and cleaning (c) Strain gauge applied to sample (d) Soldered, fully prepared samples.

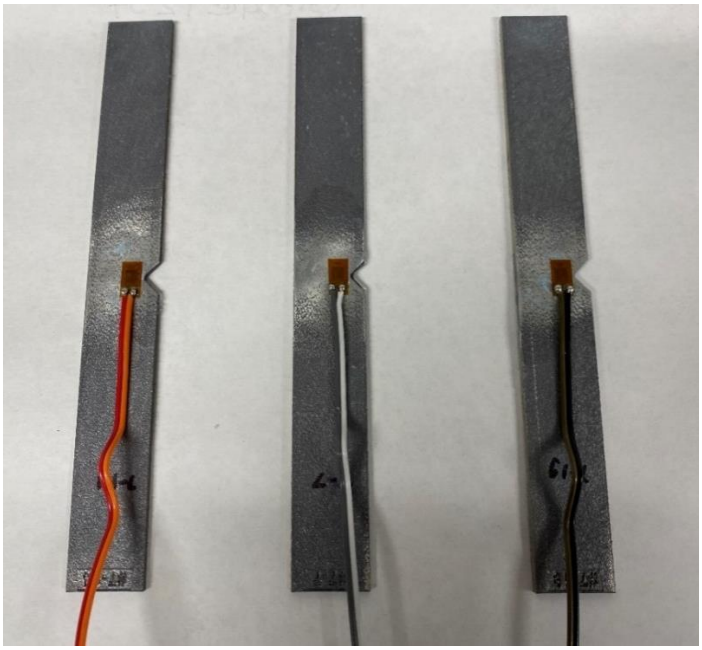

Figure 3.3: (From left to right) Samples 7-14, 7-7, 7-19 with strain gauges fully installed and ready for testing.

3.3 Strain Gauge Data Collection

After strain gauge installation, localized strain data collection requires both the appropriate software and hardware. The strain gauge lead wires are attached to a quarter bridge Wheatstone bridge circuit. A standard diagram of the circuit is shown in Figure 3.4. An image of the circuit is shown in Figure 3.5. Due to the minuscule resistance changes occurring in the foil of the strain gauge, the Wheatstone bridge circuit helps amplify the resistance change to a measurable amount. An ideal Wheatstone bridge circuit is one that is "balanced". A balanced circuit exists when all resistors are identical ($R_1 = R_2 = R_3 = R_4$); the same current flows across each leg, and therefore the original output voltage, V_0, equals zero. Resistors R_1, R_2, and R_4 used in the experiment all possess values of 350 ohms. The strain gauge replaces R_3 and has a nominal resistance of 348 ohms; this produced a nearly balanced bridge which helped in data interpretation.

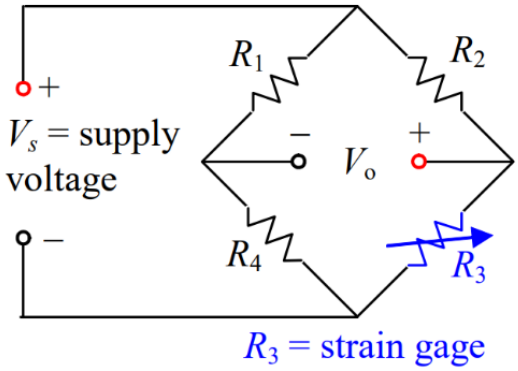

Figure 3.4: Schematic Diagram of Wheatstone Bridge Circuit.

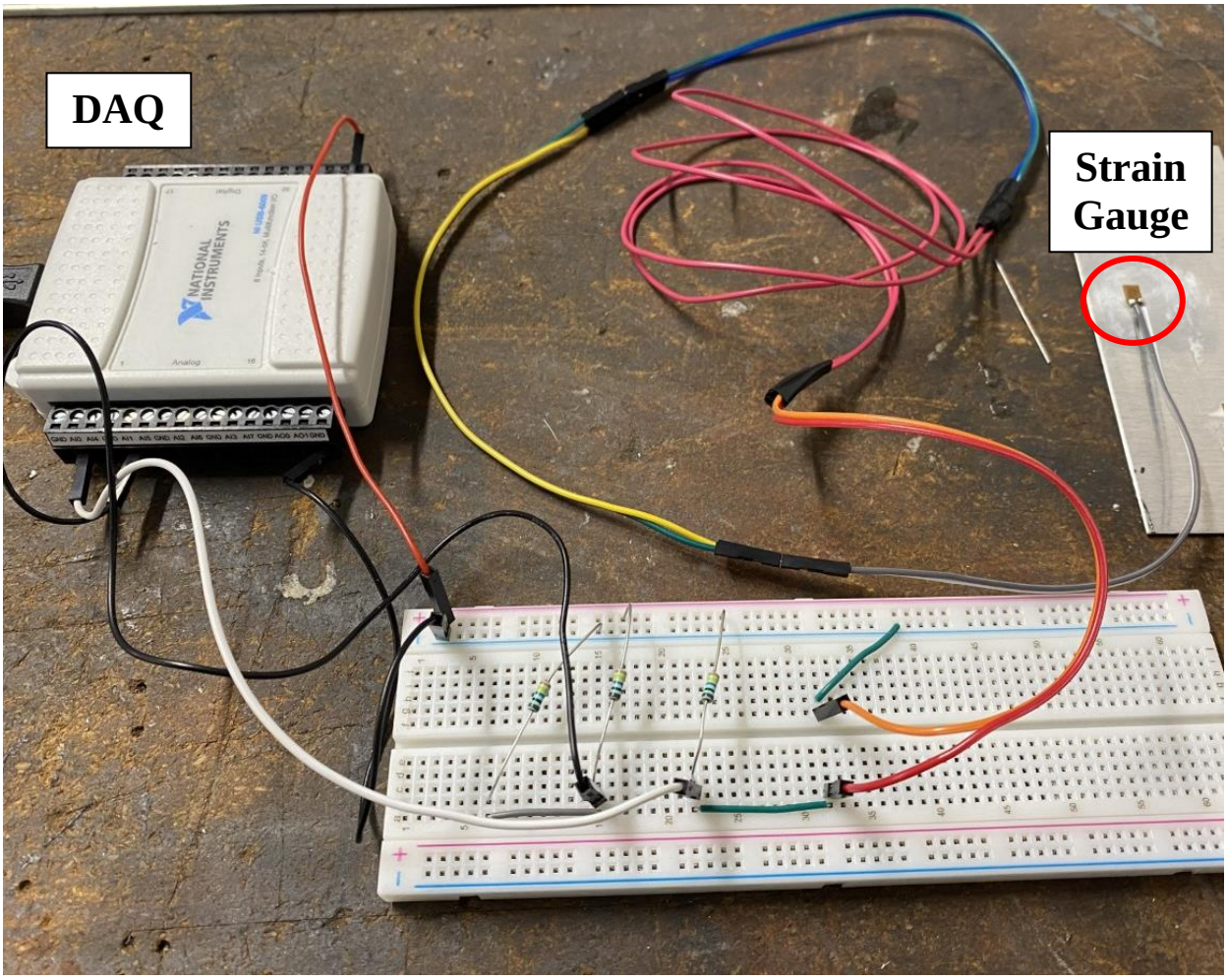

Figure 3.5: Wheatstone Bridge circuit showing connection to DAQ and strain gauge.

During testing, data is sampled at 20 Hz through a National Instruments (NI) data acquisition device (DAQ) and inputted to a MATLAB code. The NI DAQ inputs a source voltage (V_s) equal to 4.9 Volts. After traveling through all the resistors—including the strain gauge—the output voltage reenters the DAQ to be processed by the MATLAB code. The code outputs two values: a MATLAB time calculated via an internal for loop and change in voltage (V_s - V_0). The MATLAB time must be later matched up with the time recorded by the tensile testing equipment. The voltage change can then be processed into localized strain values. A sample demonstration, checking the hardware and software, resulted in Figure 3.6; this proved that the strain gauge, DAQ, and code were all properly working and ready for experimentation.

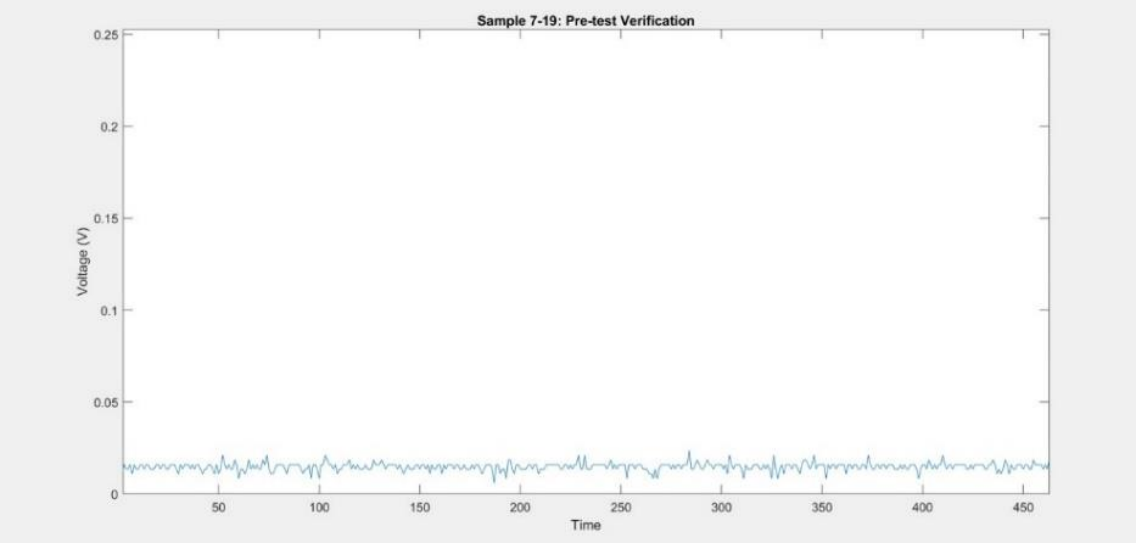

Figure 3.6: Testing MATLAB Code to ensure signal input across strain gauge.

3.4 Tensile Testing Experimentation

The tensile experiments are conducted on an MTS 50 kN electromechanical load frame shown in Figure 3.7. The sample is attached to the load frame via tension wedge grips, also shown in Figure 3.7, provided by the Materials Characterization Lab. The Materials Characterization Lab is located within the Materials Research Institute (MRI) at Penn State.

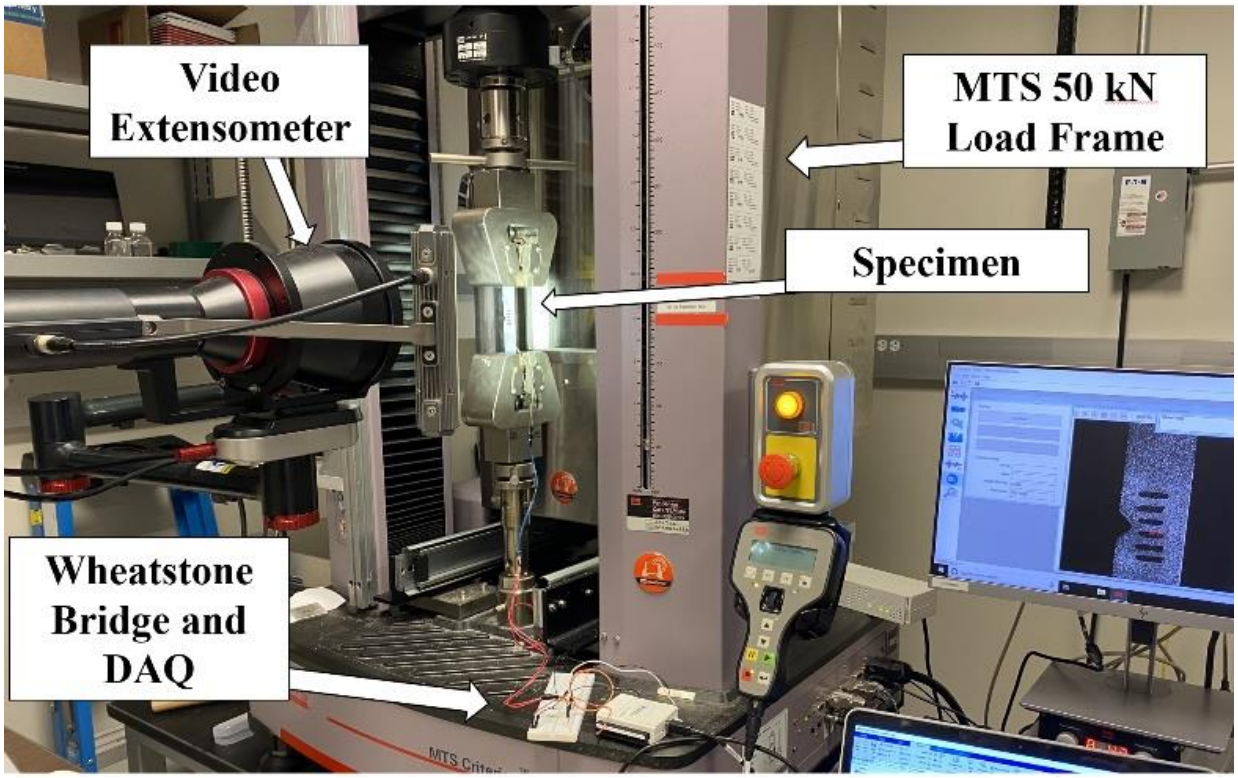

Figure 3.7: 50 kN load frame and accessory equipment at MRI.

The system incorporates several strain measuring tools and methods. As the overall crosshead position increases, it is tracked for global strain—also known as elongation—calculation. A video extensometer, equipped for tracking more localized strain, measures the average displacement across two selected points on the sample surface. The extensometer provides highly accurate localized strain. Before placement in the tensile grips, several dark lines must be drawn on the sample. The MTS Advantage™ Video Extensometer Software (AVS), utilizes these as guidelines which allow virtual crosshairs to move along with the sample surface. The AVS software relies on a finely calibrated high-resolution image; therefore, the extensometer camera and light must be perpendicular to the sample and adjusted accordingly. The extensometer setup can be seen in Figure 3.8, and the fined tuned image of the sample shown on the Video Extensometer software is shown in Figure 3.8.

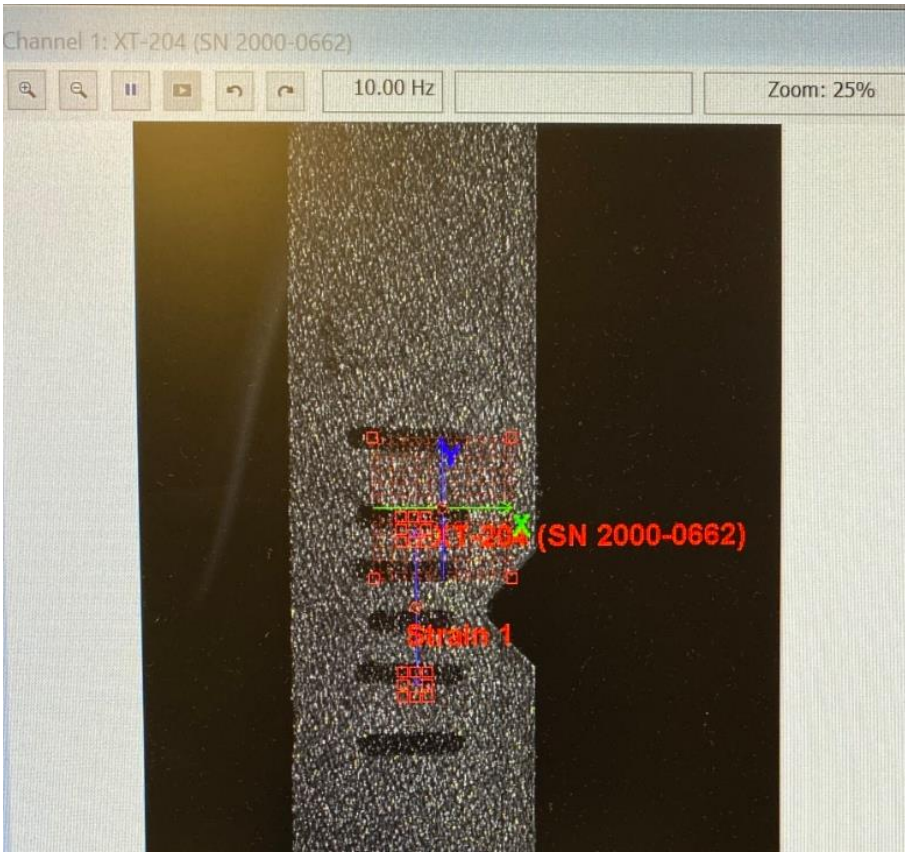

Figure 3.8: Image of AlSi10Mg sample loaded through AVS software. Notice the digital points placed on the sample to track strain.

During testing, a strain rate of 0.05 in/min is induced until complete failure (the sample is in two pieces). This is below the ASTM E8 standard (2 in/min) but ensures that the test runs long enough for proper data collection. The system records the load, strain collected via extensometer, time, and crosshead displacement throughout the entirety of the experiment. MTS TestSuite™ TW Elite is the software used to control the load frame. The software affords the user several options for testing. For ease of use and repeatability purposes, the software stores each test template. A different computer controls the video extensometer and utilizes the aforementioned MTS Advantage™ Video Extensometer (AVS) software. Lastly, a separate computer is required to run the MATLAB script which collects the strain gauge data. The order of operation is as follows: run the strain gauge script, start the extensometer, and then hit run on the MTS Load Frame.

3.5 Post-Processing

After completion of a test, there is an abundance of data for review and processing. There are two sources of data requiring different types of post-processing. The first comes from MTS Test Suite™ and the AVS video extensometer. The software outputs extensometer strain (mm/mm), load (N), crosshead position (mm), and time (s). This data produces global strain, stress, and stress-strain curves. The second source of data comes from the strain gauge code. The code outputs a .MAT file containing the voltage change across the strain gauge, and time.

Processing the raw, voltage change data into localized strain requires several steps. As seen in Figure 3.9, strain gauges record a significant amount of noise. It is important to separate the noise from the meaningful structural information. Data processing involves: first the conversion into localized strain, and second, smoothing to account for the noise. For any Wheatstone bridge circuit, Equation 1 converts the voltage change to strain.

$$\varepsilon_a = \frac{V_0}{V_s} \times \frac{1}{S} \times \frac{\left(R_2 + R_{3,initial}\right)^2}{R_2 R_{3,initial}} \tag{1}$$

In this experiment, the bridge is nearly balanced; the resistors all possess nearly the same resistance values. This results in the reduced equation for uniaxial strain shown in equation 2. The gauge factor, S, is provided via the strain gauge manufacturer. For the ED-DY-125AD-350-gauge, this factor equals 3.24.

$$\varepsilon_a = 4 \times \frac{V_0}{V_s} \times \frac{1}{S} \tag{2}$$

Equation 2 represents the simplified form to convert output voltage to strain. Importing the .MAT file into a MATLAB script allows for straightforward conversion and graphing techniques. In addition, the utilization of MATLAB provides several techniques to remove noise.

As shown in Figure 3.9, the baseline output voltage recorded by the strain gauge is not completely zero. Obviously, the sample does not experience strain prior to loading. Therefore, it is safe to

shift the baseline voltage down to zero. Any change in voltage above zero truly represents a loading event.

Viewing the plotted strain for the first time reveals a significant amount of noise; Figure 3.9 illustrates this well. Prior to loading, strain values fluctuate from negative 0.064% to positive 0.064%. The noise often displays a pattern and fluctuates around a common value. One of the most noise reduction strategies involves simply averaging. Averaging every 5 consecutive points reveals a much smoother curve and allows one to see the actual trend of the curve. In addition, this aids in truncating the data set; now samples are collected every 0.1 second compared to 0.02 seconds. Figure 3.10 shows the graph of the strain after smoothing.

A Butterworth filter via MATLAB was also considered for noise reduction; this filter produces a good ripple response but reveals a wider transition band [34]. The “butter” and “filter” command show solid filtering capability but result in too wide inconsistencies between strain gauge signals. For each signal, the filter’s transfer function—basically the settings—requires significant modification for each test compared to the averaging approach. Figure 3.10 shows a comparison between the averaging filter and the Butterworth filter.

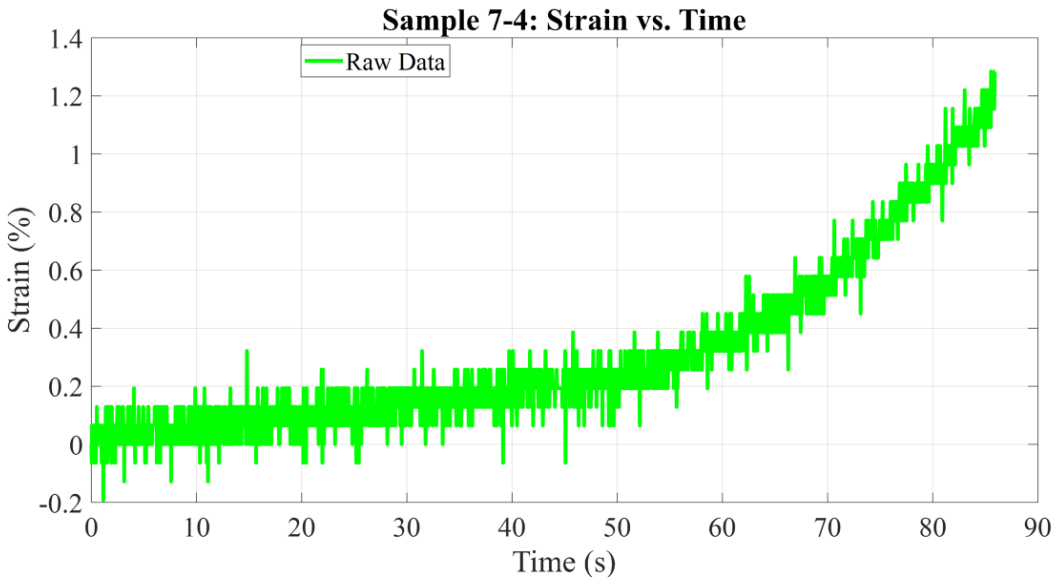

Figure 3.9: Processed strain data; before noise filtering and smoothing.

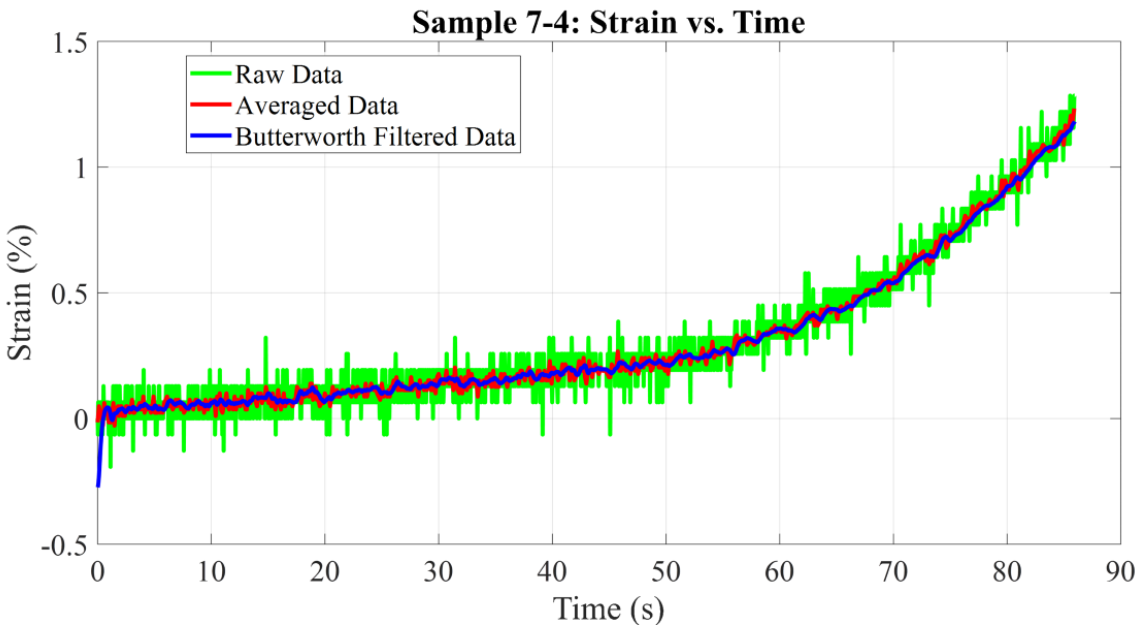

Figure 3.10: Comparison between raw, noisy data and both the averaging and Butterworth filtering methods

3.6 Stress-Strain Analysis

This section provides an overview of stress-strain processing and defines key terms used in the results section. The crosshead displacement, extensometer, and strain gauge data provide insights into the mechanical response throughout different sections of each test sample.

First, the section defines global material response throughout the entirety of the gauge region. For each test, the crosshead displaced at a specified rate until the sample broke. By dividing the change in crosshead ($\Delta\ell$) by the original gauge length (ℓ_0), one can calculate the percentage elongation for each sample. The percentage elongation accounts for the deformation throughout the entirety of the gauge region. In this thesis, this is referred to as the global response of the material. Equation 3 shows the percent elongation formula.

$$\%\, Elongation = \frac{Change\ in\ Length}{Original\ Length} \times 100 = \frac{\Delta\ell}{\ell_0} \times 100 \quad (3)$$

A proper comparison to percent elongation is the nominal stress across the unnotched portion of the sample. Throughout this thesis, this is referred to as global stress. As shown in Equation 4, stress is defined as force (F) divided by the cross-sectional area (A).

$$\sigma_{nom} = \frac{F}{A} \tag{4}$$

The second strain used for comparison is referred to as the extensometer strain. This strain is output directly via the software and requires no post-processing calculation. This data, compared to percent elongation, provides a much more accurate strain calculation. It tracks the strain near the notch region. This extensometer strain is recorded as true strain. Comparatively, the percent elongation calculation is recorded as engineering strain. True strain sums incremental elongations ($\Delta\ell_0$) and divides by the gauge length (ℓ_0) [35]. Equation 5 shows the equation for true strain similarly computed by the extensometer software. It is important to note that for small strains, like later seen in the results section, true strain and engineering strain are similar.

$$\varepsilon_{extensometer} = \sum \frac{\Delta\ell_0}{\ell_0} \tag{5}$$

The stress recorded around the notch region—the smallest cross-section—is used for the creation of stress-strain curves. For any engineering application, the maximum stress is of interest. Therefore, the stress across the notch is highlighted in the results section and calculated via Equation 6. Lastly, as outlined in the strain gauge processing section. The strain gauge strain provides the final strain comparison. In summary, “local strain” is recorded by both the extensometer and strain gauge, while the “global strain” is the percent elongation calculated by crosshead displacement.

$$\sigma_{max} = \frac{F}{A_{notch}} \tag{6}$$

3.7 Finite Element Modeling: Via Abaqus

The finite element method (FEM) is a powerful and common tool used for structural analysis applications. Utilized across a variety of industries and applications, the method first divides a specified part into small shapes referred to as elements. It then utilizes numerical techniques to iteratively solve for stress and strains across each element, and throughout the entirety of the part [36]. In this application, finite element analysis—via the software Abaqus—aims to corroborate this study's experimental findings.

The workflow within Abaqus follows the following order: defining part geometry, specifying material properties, setting constraints and interactions, designating loads, creating the mesh, and then running the simulation. Once the simulation runs successfully, one interprets the results. This next section specifies how an Abaqus simulation is run.

The part geometry is designed to match the Al6061-T6 test samples; it includes the v-notch in ordinance to the actual test samples. The sketch was extruded to a thickness of 2.29 mm. Partitions separated the gauge region from the gripping region. In addition, a reference point placed centrally on the top face defines force location. This completes the part definition portion. The part's materials properties are then assigned to match typical Al6061-T6 properties. Abaqus allows the user to assign both the young's modulus of elasticity and Poisson's ratio, which are assigned to 69,000 GPa and 0.33, respectively.

Under the interaction section, the user sets constraints for the model. A coupling constraint (which couples the motion of surface nodes to a reference node) specifies that the top cell moves rigidly with the reference point [37]. Figure 3.11 points out these regions. The load tab within Abaqus allows the user to define boundary conditions. Table 3.3 shows the three boundary conditions utilized. Essentially, the part should not rotate, the bottom region should be fixed, and top grip should only be allowed to move in the y-direction.

Table 3.3: List of Boundary Conditions (BC) applied to Abaqus model.

Region	BC Type	BC
1 - Top Grip	Displacement/Rotation	U2 = nonzero (Only allow movement in y-direction)
2 - Gauge Region	Displacement/Rotation	U2 = nonzero (Only allow movement in y-direction)
3 - Bottom Grip	Symmetry/Antisymmetry/Encastre	U1 = U2 = U3 = UR1 = UR2 = UR3 = 0 Bottom cell is fixed.

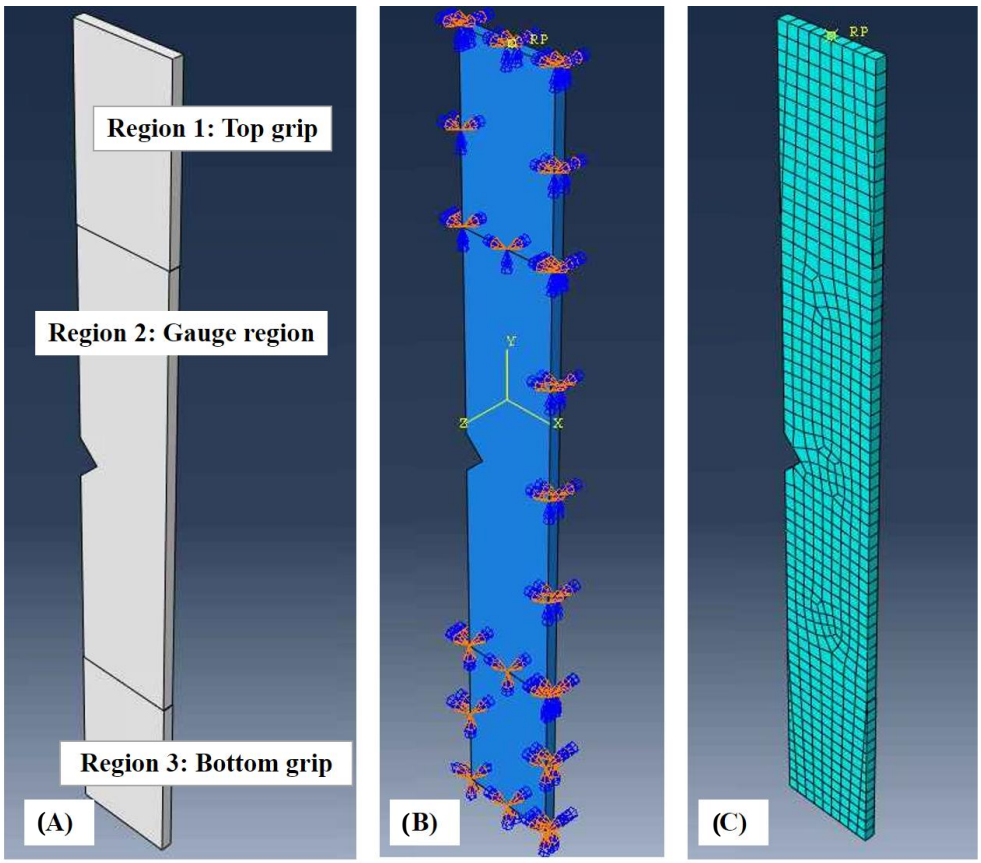

Figure 3.11: (A) Image showing definition of regions in Abaqus (B) Image showing boundary conditions applied (C) Mesh created for a representative sample

Within an Abaqus simulation, the load tab enables the user to specify loading conditions. In this study, a concentrated force is defined in the positive y-direction and set to 10,000 newtons. The force,

located at the reference point on the top face, ramps up to the max force over 10 steps. The ramp-up operates linearly from 0-1 in time and amplitude steps of 0.1. The final step before running a simulation involves mesh creation – utilizing a global seed size of 3. Once the job finishes, one can view the results directly in Abaqus, or export data into another appropriate software.

Chapter 4

Results and Discussion

The results section of the thesis outlines experimental findings from the AlSi10Mg tensile testing. First, finite element simulation results outline typical material response for aluminum alloy. Then, data from Al6061-T6 testing is shown in brevity and compared to finite element predictions–proving strain gauge accuracy with traditional materials. The thesis then reveals strength numbers of all samples, stress-strain data, and then strain-time data from both extensometer and strain gauge methods. Throughout the section, results are analyzed and compared to finite element simulations and typical results for the material. Lastly, a discussion compares the strain distributions across the material and highlights parameters that could be used for damage detection of additively manufactured materials.

4.1 Finite Element Modeling

The finite element simulations conducted via Abaqus highlighted several important features of the deformation behavior of traditional aluminum alloy (Al6061-T6). These simulations placed a load of 10,000 N on the sample. Figures 4.1 and 4.2 illustrate stress and strain distributions across the sample at this load. As anticipated, the notch geometry induces high stress and strain at the notch tip. This geometry creates a radial distribution—rings of decreasing stress and strain—outward from the notch. Figures 4.1 and 4.2 highlight the regions in which the strain gauge and extensometer sensors will track strain. At 10,000 newtons, the strain gauge should record much higher strain than the extensometer. Table 4.1 extracts the stress and strain numbers gathered via the simulation.

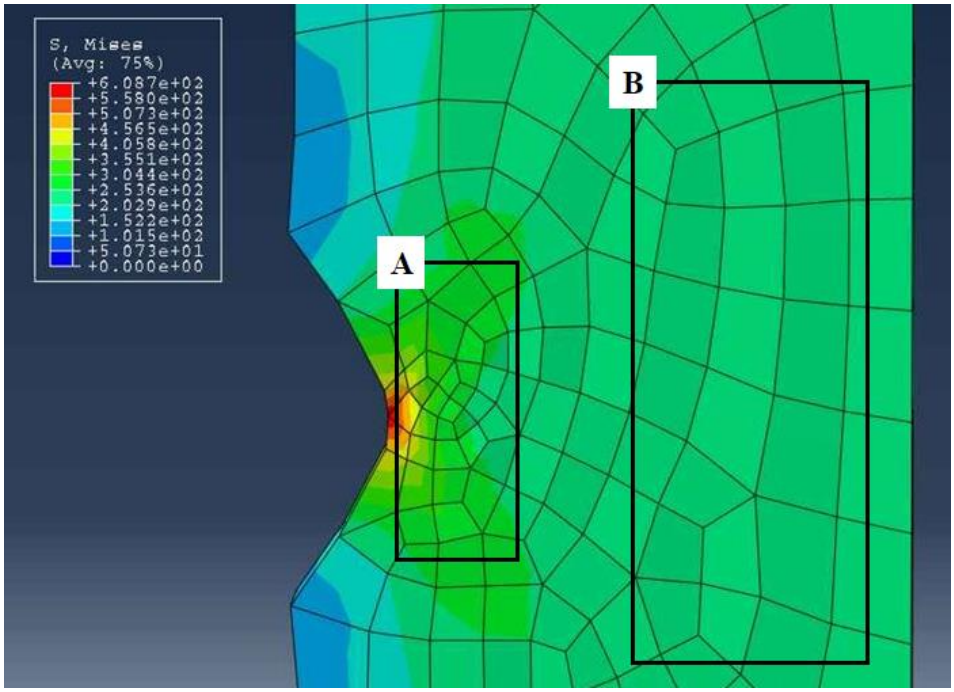

Figure 4.1: Stress distributions at 10 kN across (A) the strain gauge region and (B) the extensometer region gathered via finite element simulations.

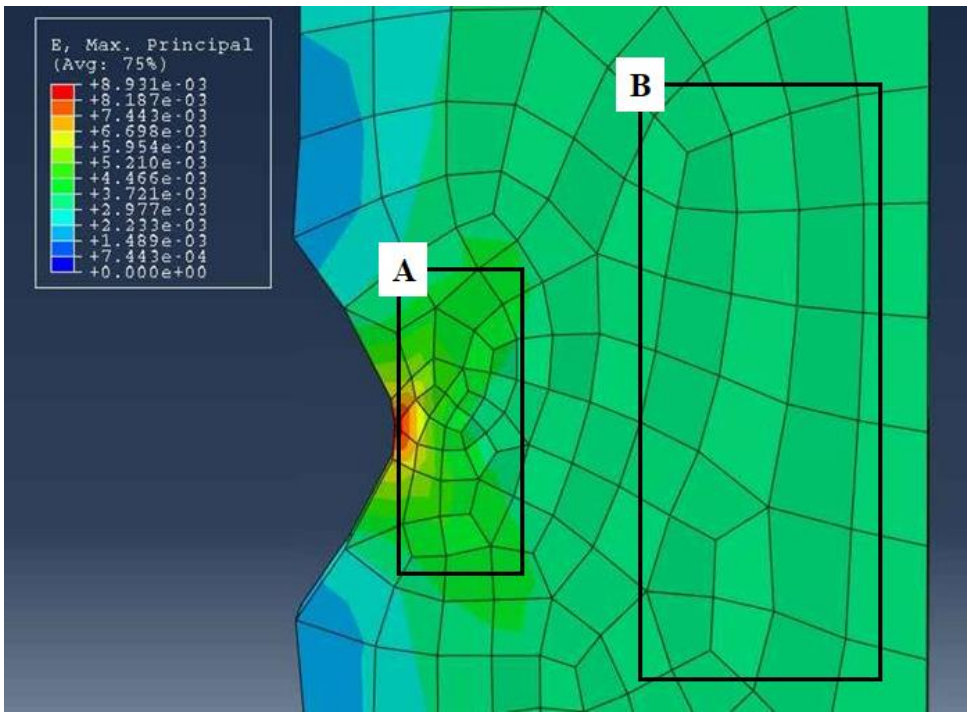

Figure 4.2: Strain distributions at 10 kN across (A) the strain gauge region and (B) the extensometer region gathered via finite element simulations.

Table 4.1: Summary of stress and strain distributions gathered via the finite element simulations shown in Figure 4.1 and 4.2

Region	Max Principal Strain (%)	Von Mises Stress (MPa)
Strain Gauge	~ 0.446 – 0.521	~3.044 – 3.551
Extensometer	~ 0.2977 – 0.372	~2.536
Percent Increase	~ 56% – 75%	~ 20.5% – 40.5%

In addition to the maximum stresses and strains, it is important to note how these distributions progress throughout the entirety of the simulation. Figure 4.3 shows the progression of the strain and overall displacement throughout the simulation. Throughout the first few steps, strain across the sample is relatively even. However, at about halfway through the simulation, the strain near the notch grows exponentially compared to the extensometer region.

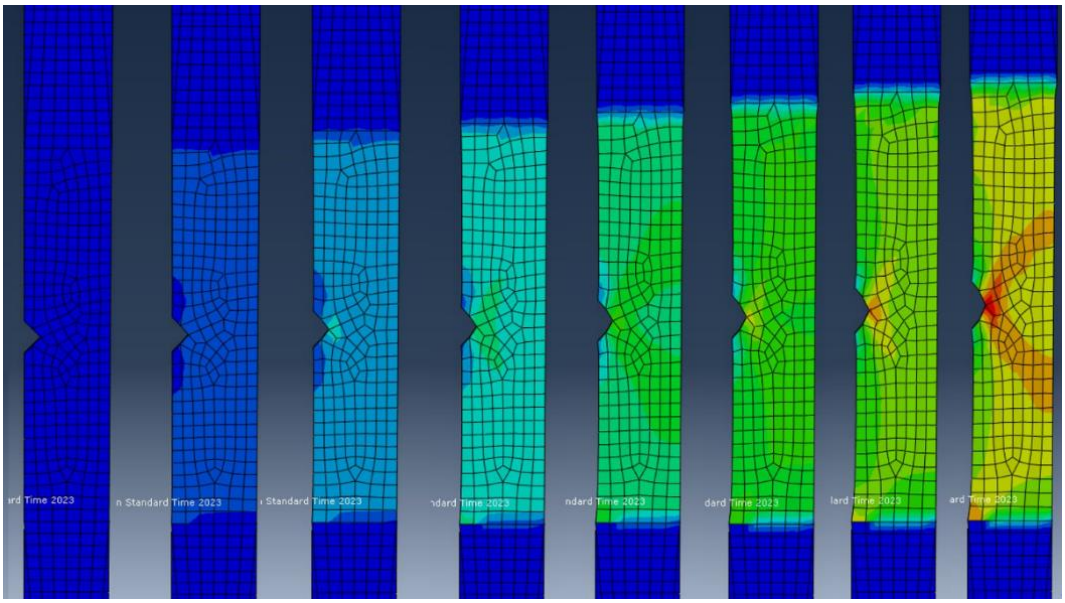

Figure 4.3: Progression of strain throughout a tensile simulation.

4.2 Testing and Verification of Al6061-T6

Prior to AlSi10Mg sample testing, Al6061-T6 samples were tested to confirm accuracy of the testing methods. The deformation behavior and ultimate strength of Al6061-T6 aluminum is widely understood. These tests produced confidence in the data analysis methods later used for the AlS10Mg samples. The production of AlSi10Mg samples is pricier compared to traditional aluminum; these tests provided means for more cost-effective strain gauge application practice. This section reviews use of several techniques to validate tensile testing methods, strain gauge data extraction, and material analysis.

The Al6061-T6 samples failed a load of 10,908 and 10,900 Newtons. This load equates to a nominal stress of 234 MPa throughout the constant cross section portions. The maximum elongation of the samples is 3.43% and 3.74%. These results are shown in Table 4.2. The stress throughout the constant cross-section plotted against the percent elongation is shown in Figure 4.4. These results are further discussed when compared to the local data.

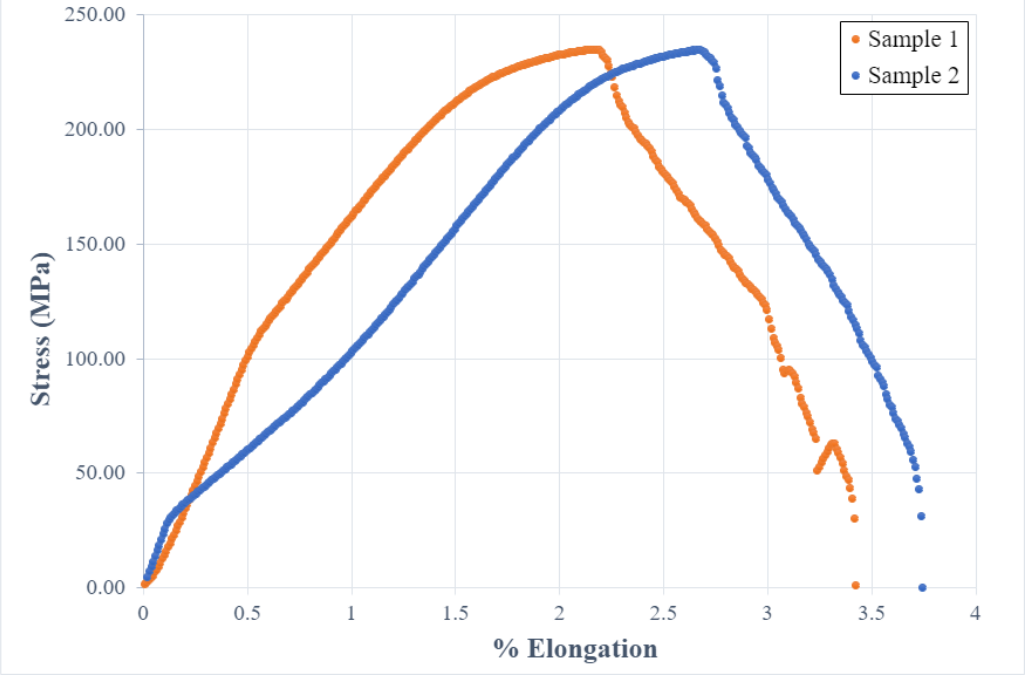

Figure 4.4: Graph comparing percent elongation with stress across the unnotched, constant cross-section region of the Al6061-T6 samples.

Table 4.2: Global Test Data of Al6061-T6 Samples.

Sample ID	Max Load (N)	Unnotched Area (mm^2)	Stress (MPa)	Elongation
1	10908.79	46.487	234.66	3.43%
2	10900.89	46.487	234.44	3.74%

Test data collected via digital extensometer provides a more precise insight into the mechanical response of the material; it directly tracks the strain across the notch region. Percent elongation, while effective, is a drastic simplification of strain. In our case, the v-notch stress concentration means that this simplification is not completely effective. The v-notch guided the crack growth and failure of the sample. Dividing the maximum load by the cross-sectional area across the notch reveals an ultimate strength of 292 MPa. Typical Al6061-T6 ultimate tensile strengths lie at 310 MPa. This number is likely reduced during these experimental tests due to the notch geometry.

Table 4.3 shows the samples 1 and 2 experienced maximum strains of 5.66% and 10.3%, respectively. Figure 4.6 shows that sample 1 has an abbreviated stress-strain curve compared to sample 2. However, as shown in Table 4.4, both samples nearly had the same modulus of elasticity. As mentioned in the introduction section, both Al6061-T6 samples experience the same mechanical response. An engineer could robustly design with this material.

Table 4.3: Extensometer Test Data of Al6061-T6 Samples

Sample ID	Max Load (N)	Notched Area (mm^2)	Max Stress (MPa)	Max Strain
1	10908.79	37.33	292.25	5.66%
2	10900.89	37.33	292.04	10.3%

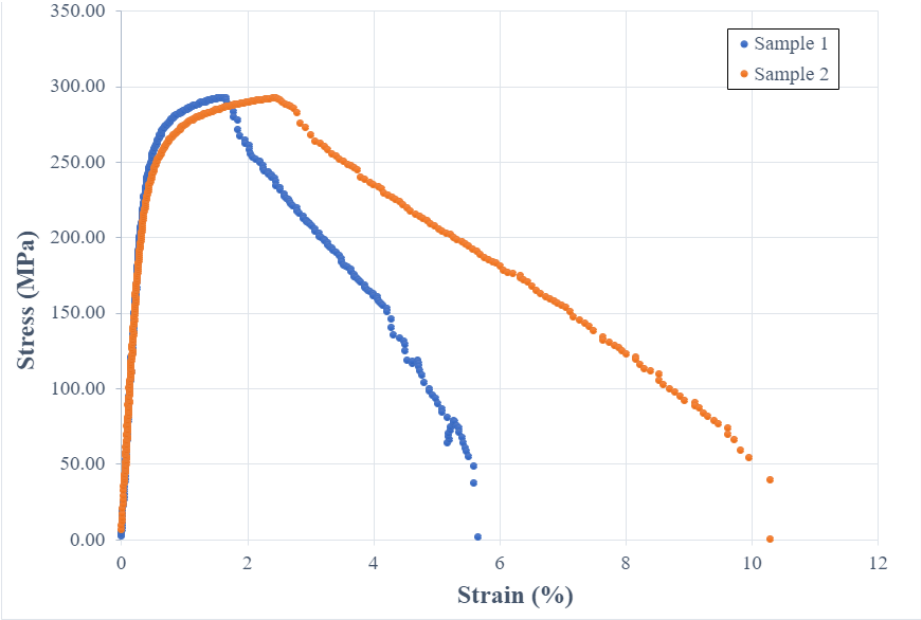

Figure 4.5: Graph comparing stress across notch of a representative Al6061-T6 sample with strain calculated via extensometer.

Table 4.4: Elastic modulus of Al6061-T6 samples calculated via extensometer

Sample ID	Elastic Modulus (GPa)
1	69.99
2	70.65
Known Reference [31]	**69.0**

4.2.2 Comparison of Strain Gauge and Extensometer Strain

The strain recorded via extensometer—near the notch region—is significantly higher compared to percent elongation for both samples. The notch creates a high deformation region. Traditional aluminum alloy is a ductile material. While giving a pathway for crack growth, the notch does not completely reduce the material's ductility. As seen in Figure 4.6, the material experiences strain hardening and necking.

Figures 4.6-4.7 compare the strain collected via strain gauge to strain collected by the extensometer. As predicted by the finite element simulations, the strain gauge records higher strain than the extensometer due to its proximity to the notch tip. The progression of the strain over the time of the experiment follows three portions: linear matching, exponential deviation, and failure. During the linear matching portion (roughly the first 10 to 15 seconds), the strain gauge and extensometer lines follow each other closely, and linearly. In this section, the strain throughout the notch region is roughly uniform. When compared to the raw data set, which shows force vs. time, this occurs up to a force 8,000 Newtons for sample 1 and 4,500 Newtons for sample 2.

The exponential deviation portion occurs when the strain recorded by the gauge no longer matches the extensometer. In this portion, the strain stops increasing linearly and becomes exponential. The strain gauge strain increases exponentially faster compared to the extensometer. The strain gauge is experiencing high stresses and strains; the stress concentration is basically directly on the gauge. This portion occurs until strain gauge failure. During these experimental tests, the crack propagates directly through the center of the gauge. At this point, the gauge loses its signal. In figures 4.7-4.8, this moment is shown when the line stops. For sample 1, this occurred at 21.2 seconds and a load of 10,763 newtons. The gauge on sample 2 lost connection at 20.7 seconds and a load of 9375 newtons. The extensometer curve continues to grow exponentially while the crack propagates, and the sample continues to neck. These three strain progression terms are utilized during the analysis of the AlSi10Mg samples in the next portion of the thesis.

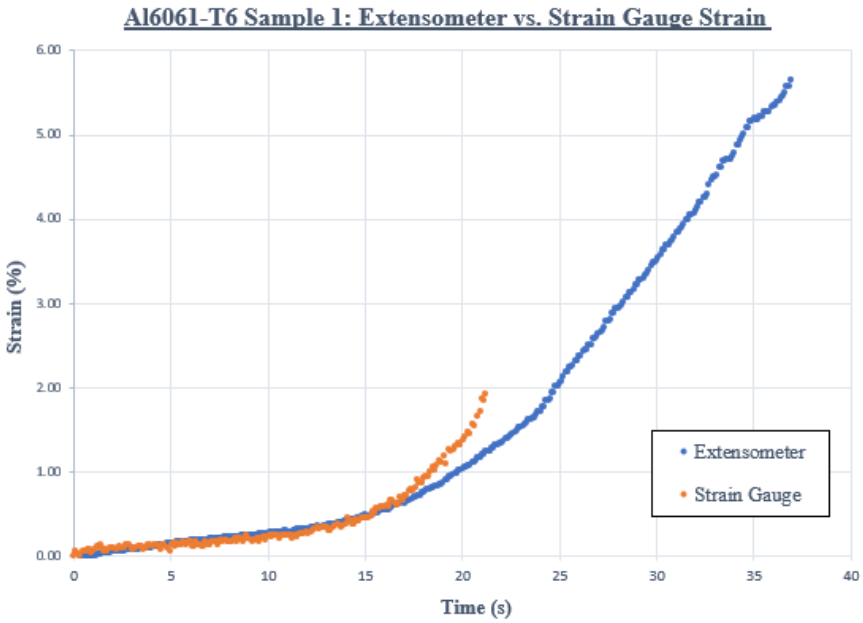

Figure 4.6: Comparison of strain detected via strain gauge vs. extensometer for Al6061-T6 sample 1.

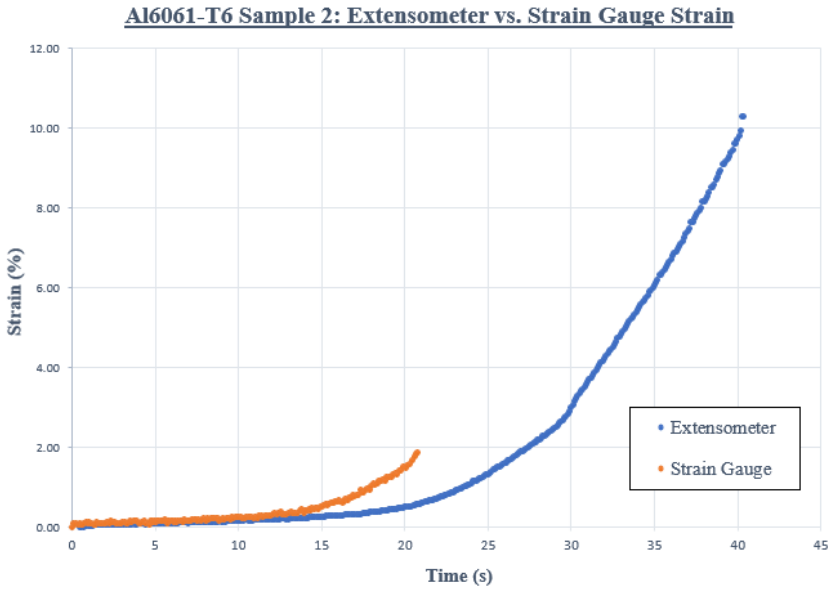

Figure 4.8: Comparison of strain detected via strain gauge vs. extensometer for Al6061-T6 sample 2.

4.3 Testing of L-PBF AlSi10Mg Samples

The study tested 6 different AlSi10Mg samples manufactured via L-PBF with strain gauges attached to the surface. While the Al6061-T6 testing laid the groundwork, these tests lead to results pertinent to the research surrounding L-PBF AlSi10Mg. This section involves four main thrusts: reporting global stress and elongation data, extensometer localized stress and strain, strain gauge strain, and finally a discussion on the strain distribution throughout the sample.

4.3.1 Unnotched Stress and Global Elongation Data

This section will briefly summarize global material response. The failure load, nominal stress, and percent elongation for each sample is shown in Table 4.5. The range of failure loads and stresses is somewhat striking. The stresses range from 157.11 to 188.77 MPa; this is roughly an 18% difference. The range of percent elongation is also significant, but considering literature, is more expected. Even the Al6061-T6 samples had slight differences within elongation. The global stress-strain (referred to as elongation in the figure) curves are shown in Figure 4.7. At first glance, these curves show an extreme lack of ductility. Previous literature shows that L-PBF AlSi10Mg samples typically break at their respective ultimate strengths without any necking. The curves shown in Figure 4.11 completely lack strain hardening and necking regions. It is important to note that no visual crack growth appeared during the test, and the sample experienced brittle failure. Likely, the notch geometry induced a high stress concentration causing the sample to lose all ductility and fracture after its first defect grew to a substantial size.

Table 4.5: Summary of maximum loads and maximum stresses experienced by AlSi10Mg samples in constant cross section portions.

Sample ID	Test Rate (in/min)	Failure Load (N)	Nominal Stress (MPa)	Elongation (%)
7-4	0.05	7,916.16	185.56	2.05
7-6	0.5	6,623.5	157.11	1.59
7-7	0.05	6,915.62	170.55	1.86
7-11	0.05	6,677.43	162.19	1.97
7-14	0.05	6,502.88	159.66	1.55
7-19	0.05	7,512.85	188.77	2.08

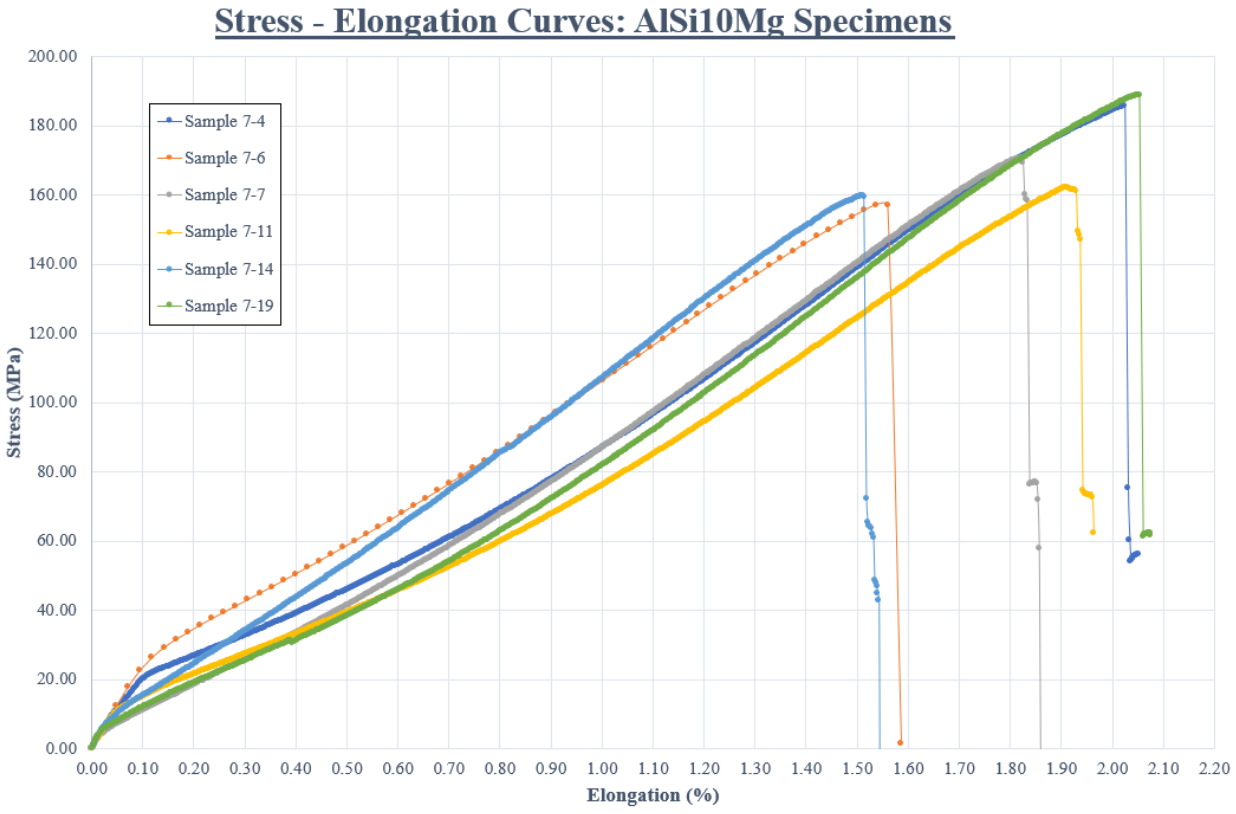

Figure 4.7: Global stress and elongation curve for constant cross-section AlSi10Mg samples.

4.3.2 Notched Stress and Extensometer Strain Data

As discussed with the traditionally manufactured aluminum samples, the digital extensometer provides more precise insight into the mechanical response of the material. Global elongation data clarifies the big picture but is not completely useful in providing ultimate strength numbers, strains, or curves. The extensometer provides the true behavior of the material and outputs more accurate stress-strain curves.

Table 4.6 shows the maximum load, stress, and strain of each sample experienced during testing. The max stress ranges from 197.13 MPa to 236.5 MPa; this is roughly an 18% difference. The maximum strain ranges from 0.61% to 1.02%; this is roughly a 50% difference. This is extremely inconsistent, however the traditional aluminum samples also experienced different maximum strains. Indicated by the low strain results, these samples are extremely brittle, and they fractured without any visual crack growth. The stress-strain curves of each sample are shown on the same axis in Figure 4.8.

Table 4.6: Summary of maximum stress (across notch) and strains

Sample ID	Test Rate (in/min)	Failure Load (N)	Max Stress (MPa)	Max Strain (%)
7-4	0.05	7,916.2	232.97	0.75
7-6	0.5	6,623.5	197.13	0.70
7-7	0.05	6,915.6	213.78	0.63
7-11	0.05	6,677.4	203.52	1.02
7-14	0.05	6,502.9	200.15	0.61
7-19	0.05	7,512.9	236.55	0.67

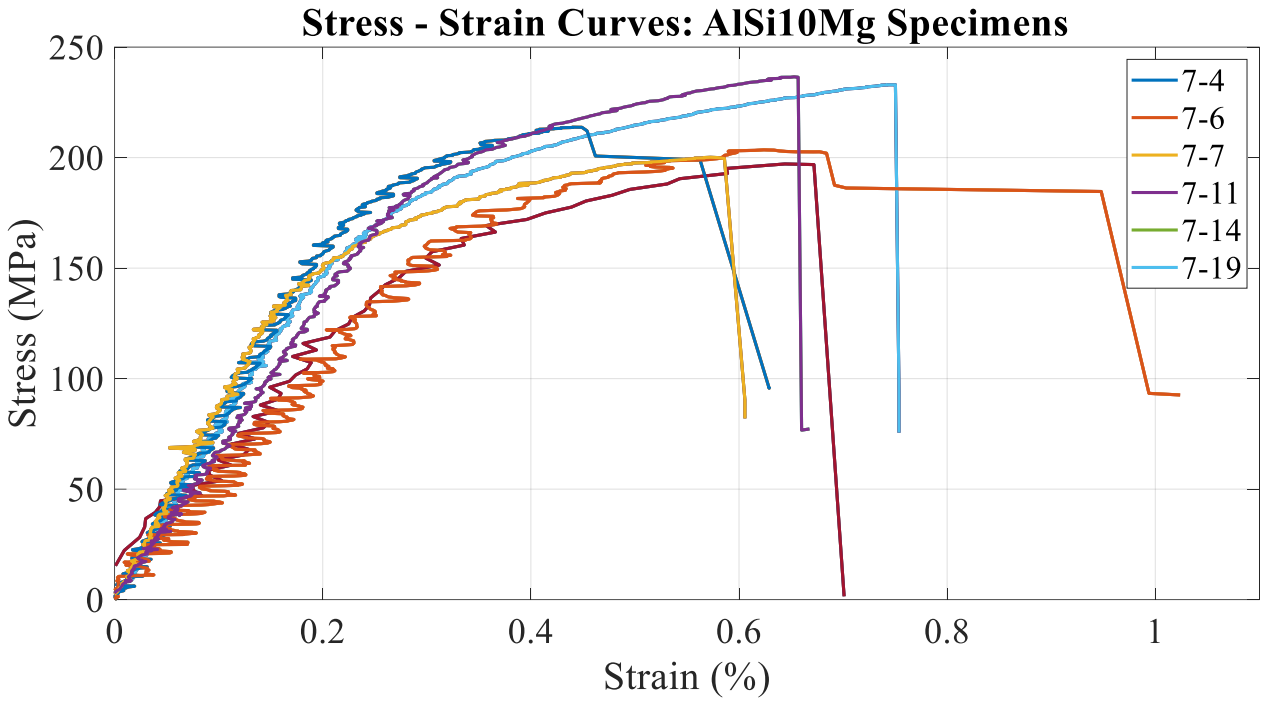

Figure 4.8: Stress-strain curves for each AlSi10Mg sample. The stress is the max stress recorded across the notch. The strain is recorded via extensometer.

The extensometer's stress-strain curves, in comparison to the global curves, follow more typical results for AlSi10Mg manufactured via LPBF. These curves exhibit a strain hardening region, but still an abrupt failure with no necking. Another important comparison to the global curves involves the max strain recorded. The percentage elongation is higher than the extensometer strain. This is opposite from the aluminum samples. In addition, on a sample-by-sample basis, the max strain had little correlation with percent elongation. The hypothesis for these differences are discussed in the following section. Figure 4.9 shows each graph on a separate axis for another comparison.

The zig-zag shape of the stress-strain curves is another interesting note. The according to literature, the "zig-zagging", associated with stress or strain drops, is commonly known as serration behavior [38]. It is common in Al-Mg alloys. However, it usually occurs only during plastic deformation. Many studies focus on this behavior; however, it is not a main thrust of this thesis.

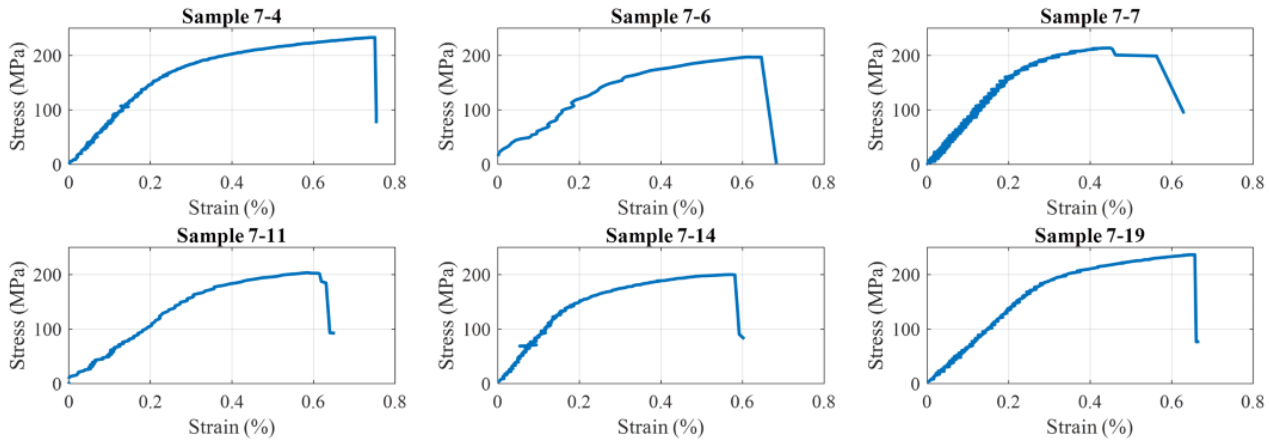

Figure 4.9: Stress-Strain curves for each L-PBF AlSi10Mg sample tested.

4.3.3 Comparison of Strain Gauge and Extensometer Strain

This section presents the comparison between strain collected via strain gauge and extensometer. Figures 4.10-4.15 show these comparisons. As previously mentioned, the progression of the strain over the time of the experiment follows three portions: linear matching, exponential deviation, and failure. For the additive tests, these portions remain nearly the same. The failure portion of the curve—where the strain gauge disconnects and fails, but the sample continues to strength—is non-existent. Because the samples are extremely brittle, the strain gauge fails at sample completely fails. The sample completely shattered through the strain gauge, cutting the connection. At failure, the strain gauge records higher strain compared to the extensometer. In addition, the linear matching portion of the graph occurs at different lengths between samples. These points of deviation will be recorded in Table 4.7.

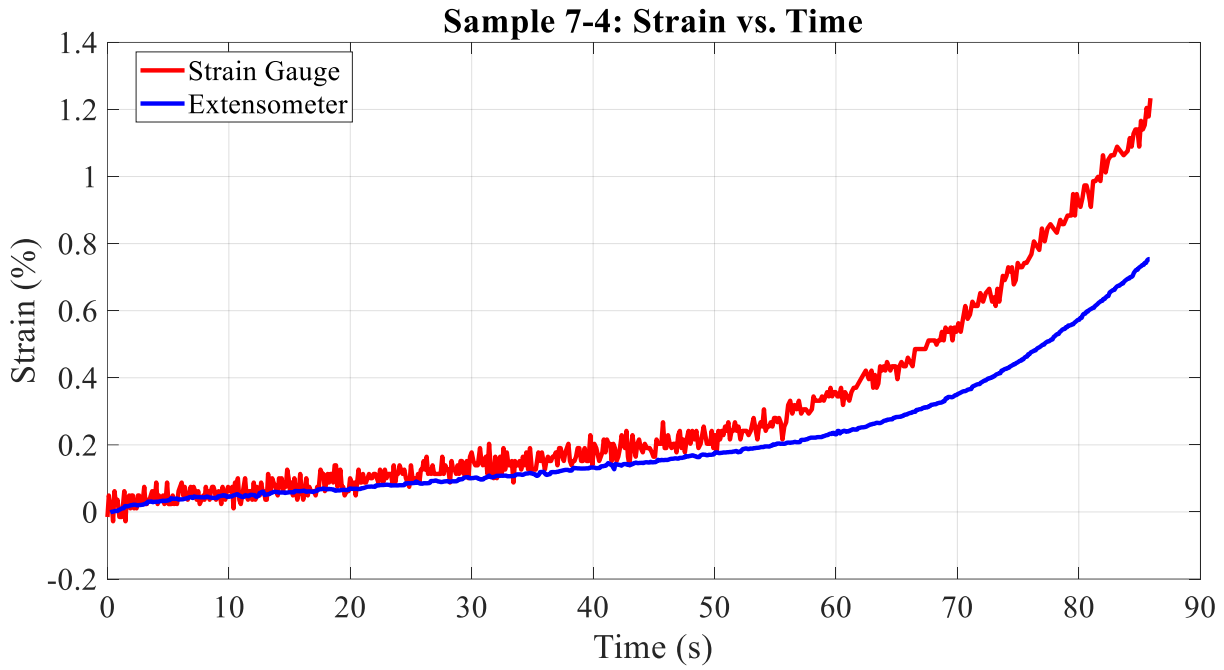

Figure 4.10: Comparison between strain recorded via extensometer and strain gauge sensor for Sample 7-4.

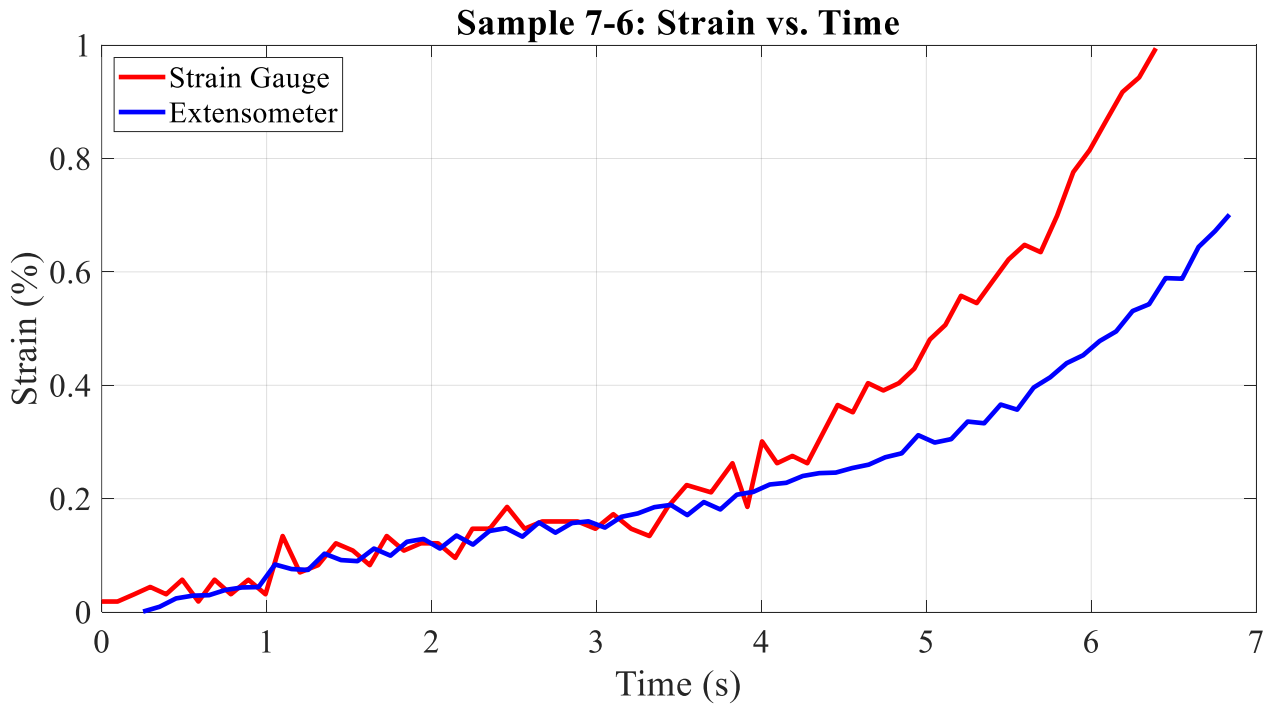

Figure 4.11: Comparison between strain recorded via extensometer and strain gauge sensor for Sample 7-6.

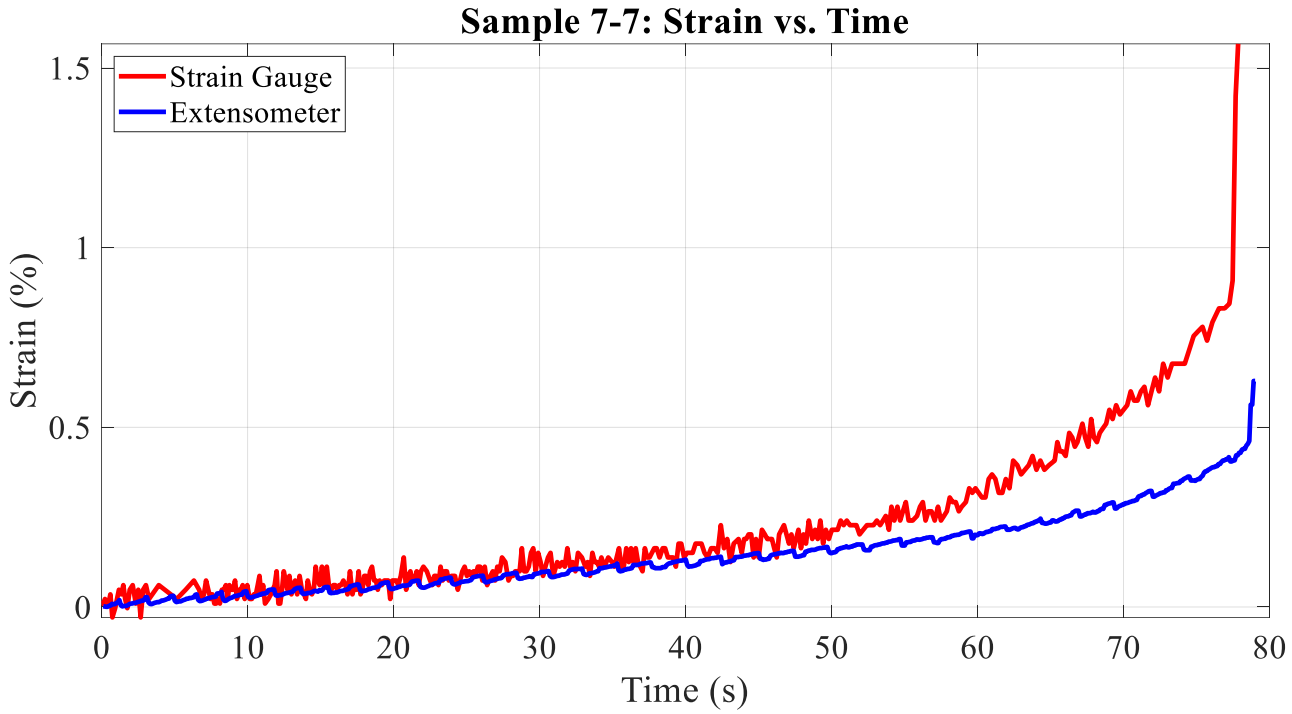

Figure 4.12: Comparison between strain recorded via extensometer and strain gauge sensor for Sample 7-7.

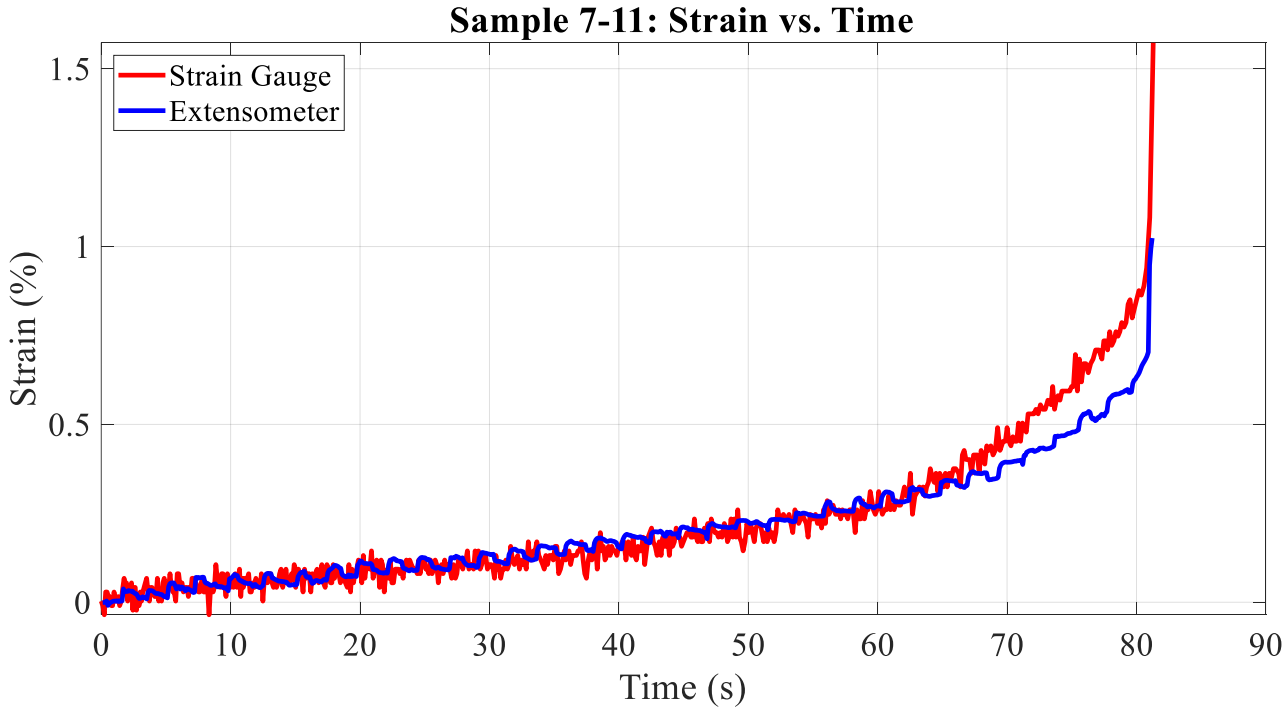

Figure 4.13: Comparison between strain recorded via extensometer and strain gauge sensor for Sample 7-11.

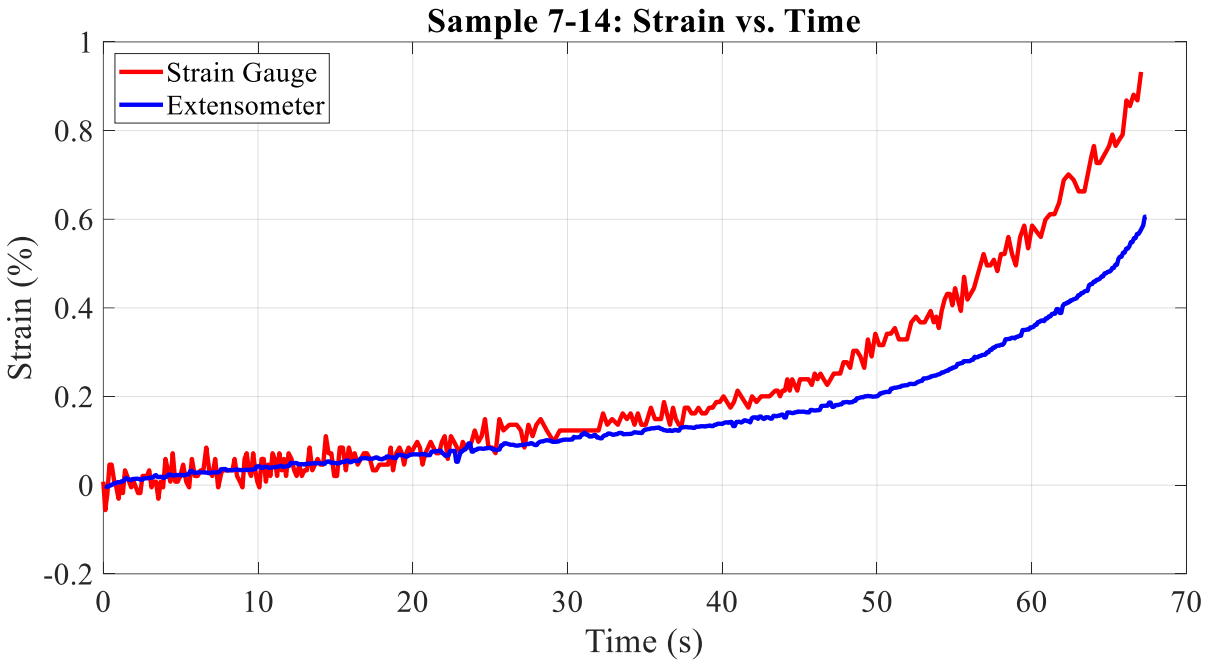

Figure 4.14: Comparison between strain recorded via extensometer and strain gauge sensor for Sample 7-14.

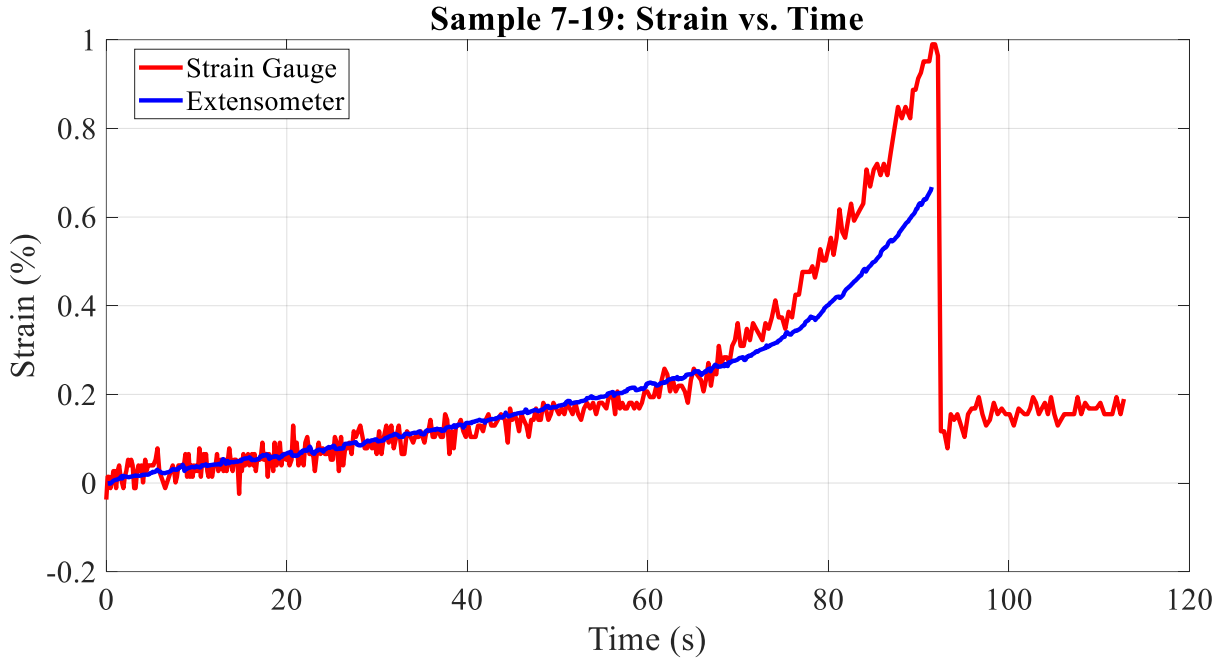

Figure 4.15: Comparison between strain recorded via extensometer and strain gauge sensor for Sample 7-19.

Table 4.7 points out where the strain collected via strain gauge deviates from the extensometer strain. Visually looking at the table reveals inconsistencies, however, graphically plotting these points on

each samples stress-strain curve uncovers a different story. Figure 4.16 shows that the point at which the strain gauge strain becomes non-linear matches with the yield stress of each stress-strain curve.

Table 4.7: End of linear matching portion - point where extensometer and strain gauge data deviate - for each AlSi10Mg sample

Sample ID	Time (s)	Strain (%)	Load (N)	Stress (MPa)
7-4	52.24	0.18	4699	138.3
7-6	3.451	0.189	3605	107.3
7-7	49.31	0.164	4134	127.8
7-11	62.23	0.298	5063	154.3
7-14	37.31	0.129	3622	111.5
7-19	67.76	0.262	5519	173.8

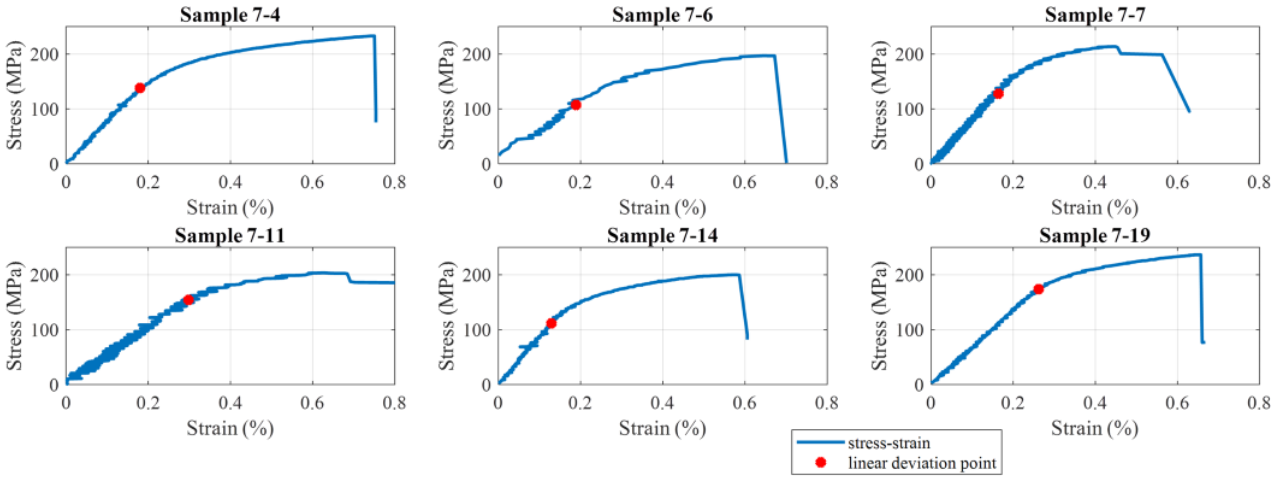

Figure 4.16: Stress-strain curves with strain gauge non-linearity point highlighted. One can see it nearly matches with the yield stress for each sample.

Figure 4.16 shows that the beginning on strain gauge nonlinearity marks the beginning of plastic deformation and the indication of the sample yielding. By many design standards, the yield stress of a material is used as the criteria for failure. According to solid mechanics, loading past the yield stress

results in plastic and permanent deformation. These results are significant because the strain gauge essentially detected the failure of each sample regardless of that sample's strength. Although the strength, and even ductility of each sample varies, the strain gauge cut through material differences and highlighted the failure point during each test.

4.3.4 Strain Distribution Discussion

The strain distribution throughout the AlSi10Mg samples—recorded through both extensometer and strain gauge sensors—matched finite element simulations. Table 4.8 lists the maximum local strains collected with extensometer and strain gauge, and the global strain collected via elongation calculation. As previously mentioned, the global elongation is higher than the local strain. This is due to the sample's brittle characteristics. During the experimental testing of a ductile material, such as the Al6061-T6 aluminum, the local strain outruns the global elongation during the necking portion of the test. With the brittle AlSi10Mg sample, the material does not neck and therefore the local strain does not have the chance to catch up to the global percent elongation. These Al6061-T6 and AlSi10Mg comparisons can be seen in Figures 4.17 and 4.18, respectively.

Table 4.8: List of maximum strain collected via strain gauge, extensometer, and elongation calculation.

Sample ID	Max Strain Gauge Strain (%)	Extensometer Strain (%)	Elongation (%)
7-4	1.282	0.75	2.05
7-6	1.084	0.70	1.59
7-7	1.084	0.63	1.86
7-11	1.621	1.02	1.97
7-14	1.009	0.61	1.55
7-19	1.066	0.67	2.08

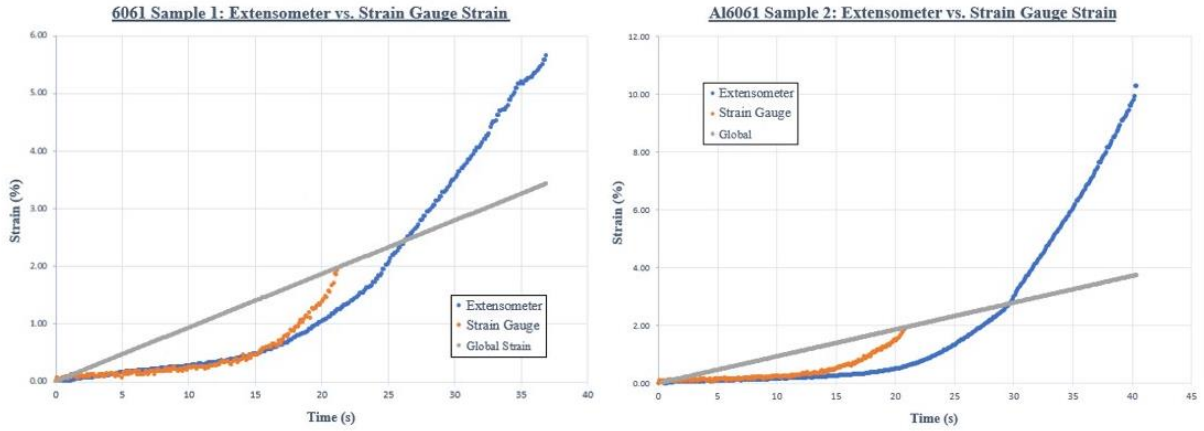

Figure 4.17: Strain gauge, extensometer, and global strain vs. time curves for ductile Al6061-T6 samples

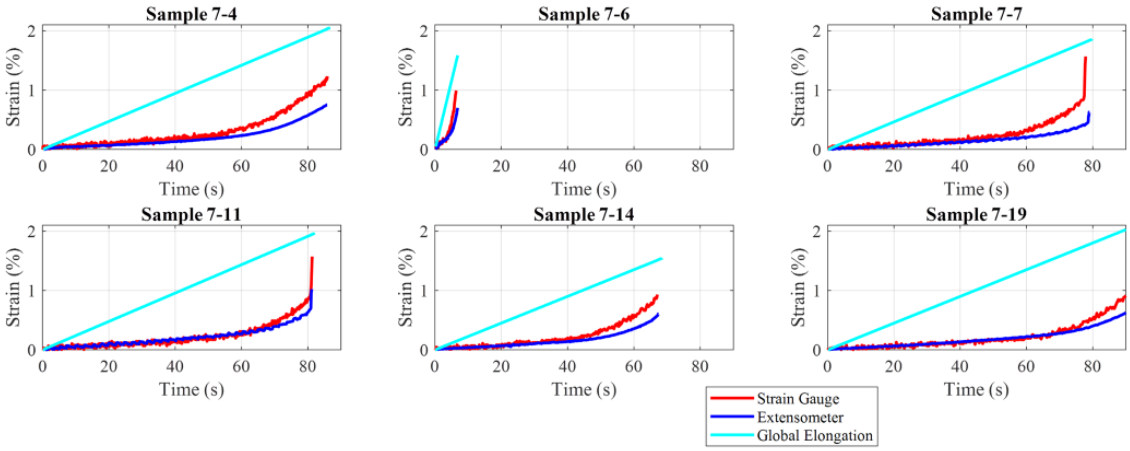

Figure 4.18: Comparison between strain gauge, extensometer, and global strain in each AlSi10Mg sample. The local strain never catches up to the percent elongation due to the lack of material ductility.

A numerical comparison is shown in Table 4.9. It shows that the percent increase in strain from the extensometer region to strain gauge region varies from approximately 55% to 72%. This matches the finite element simulations which predicted roughly a 55% to 75% increase from the extensometer region to the strain gauge region. This proves that the strain gauges accurately recorded the strain in the additive sample.

Table 4.9: Percent increase from strain gauge strain to extensometer strain

Sample ID	Ext. Strain (%)	Strain Gauge Strain (%)	% Increase
7-4	0.75	1.282	70.93
7-6	0.70	1.084	54.85
7-7	0.63	1.084	72.06
7-11	1.02	1.621	58.82
7-14	0.61	1.009	65.40
7-19	0.67	1.066	59.10

Chapter 5

Conclusion

5.1 Research Summary

The main thrust of the research involved application of strain gauges on additively manufactured materials. Up to this point, relatively few studies exist coupling strain gauge sensors with mechanical testing on additive materials. The second thrust involved testing the mechanical strength of notched L-PBF AlSi10Mg samples. The results of the mechanical tests, in terms of stress and strain, yielded highly inconsistent results. Ultimate tensile strengths ranged from 197.13 MPa to 236.5 MPa—roughly an 18% difference. Extensometer strain and global elongation capability also highly varied; these ranged from 0.61% to 1.02% and 1.55% to 2.08% respectively. Clearly, significant research should focus on printing parts with consistent mechanical properties. These mechanical inconsistencies likely stem from a heterogeneous microstructure throughout the sample. It is understandable why industry is hesitant to widely utilize additive materials such as L-PBF AlSi10Mg for structural applications.

These mechanical performance inconsistencies highlight the need for appropriate and accurate monitoring systems for additively manufactured materials. In this study, strain gauges were installed in close proximity to a notch—designed to create an unequal stress distribution and concentration—and utilized to monitor the integrity of the material during the tension tests. Prior to the tension tests, Abaqus finite element simulations predicted an annular stress and strain distribution. The strain gauge accurately tracked higher localized strain compared to the extensometer due to proximity to the notch. This study demonstrated that strain gauges can successfully be installed to poor surface additive materials and utilized to accurately monitor a material.

The comparison of the strain gauge strain with the extensometer strain over the time of the experiment returned significant results. The strain progression over the time of the experiment follows linear matching until exponential deviation and failure. In this linear matching portion, the strain near the notch increases linearly. This linear region is associated with the elastic regime of the material. However, the transition to non-linear, and exponential growth marks the transition into the plastic regime. The structures community widely recognized this region as “failure”. Essentially, the strain gauge properly monitored and detected damage of the material prior to catastrophic failure. Although each sample demonstrated different strength capabilities, the strain gauge provided robust detection of the materials yield strength.

5.2 Limitations

This study also contains several limitations which need to be addressed. First, it should be noted that the stress-strain curves reported in the study are not a complete representation of material capability for all L-PBF AlSi10Mg. The material composition and printing parameters for every L-PBF AlSi10Mg should be meticulously noted. Many research studies currently focus on optimizing laser powder bed fusion process parameters and material composition. Therefore, the stress-strain data presented are not completely representative of all of the different forms of this particular material.

This study required heavy post-processing of strain gauge data to accomplish the graphs seen in the results section. It is important to remember this data was filtered; there may be a slight error due to the noise recorded during testing. Regardless of the noise, they adequately identified the failure of each sample. One must identify extreme caution in separating noise from structural information.

5.3 Recommendation for Future Works

This research opens the door for several other research projects involving structural health monitoring and damage detection of additive materials via strain gauges. Most of the comparisons discussed in this thesis were qualitative. The terms linear and nonlinear portions of the curve were talked about in detail, and the deviation points were determined qualitatively. In the future, curve fitting or machine learning algorithms could precisely identify the beginning of plastic deformation. Obviously, algorithms aid in more streamlined structural monitoring and damage detection.

As discussed in the literature review, L-PBF AlSi10Mg samples typically contain both microstructural and mechanical inconsistencies throughout a sample. An interesting opportunity for future work involves installing strain gauges in different portions of a constant cross-section sample (such as a dog bone). It would be valuable to create strain field models throughout the sample and note where it fails.

Analyzing and tracking damage due to cyclic loading, and fatigue offers another opportunity for research. AM materials often display a largely reduced fatigue strength compared to their traditional counterparts. Therefore, there is a necessity for establishing damage detection methods over the life of a part. This may prove challenging for strain gauges due to both their noise, and the shear amount of data they tend to collect.

Finally, further strain gauge data processing should be researched. Strain gauges tend to be accurate, cheap, and useful for application in small spaces. However, the main drawbacks tend to involve the heavy data processing they require. They often sample at extremely high rates—creating massive datasets—and exhibit a strong amount of noise which at times is hard to distinguish from meaningful structural information.

BIBLIOGRAPHY

[1] B. Blakey-Milner *et al.*, "Metal additive manufacturing in aerospace: A review," *Mater Des*, vol. 209, p. 110008, 2021.

[2] J. Lettori, R. Raffaeli, M. Peruzzini, J. Schmidt, and M. Pellicciari, "Additive manufacturing adoption in product design: An overview from literature and industry," *Procedia Manuf*, vol. 51, pp. 655–662, 2020.

[3] T. Pereira, J. v Kennedy, and J. Potgieter, "A comparison of traditional manufacturing vs additive manufacturing, the best method for the job," *Procedia Manuf*, vol. 30, pp. 11–18, 2019.

[4] Y. Zhang *et al.*, "Additive manufacturing of metallic materials: a review," *J Mater Eng Perform*, vol. 27, no. 1, pp. 1–13, 2018.

[5] W. E. King *et al.*, "Laser powder bed fusion additive manufacturing of metals; physics, computational, and materials challenges," *Appl Phys Rev*, vol. 2, no. 4, p. 041304, 2015.

[6] D. Svetlizky *et al.*, "Directed energy deposition (DED) additive manufacturing: Physical characteristics, defects, challenges and applications," *Materials Today*, vol. 49, pp. 271–295, 2021.

[7] M. Li, W. Du, A. Elwany, Z. Pei, and C. Ma, "Metal binder jetting additive manufacturing: a literature review," *J Manuf Sci Eng*, vol. 142, no. 9, 2020.

[8] P. K. Gokuldoss, S. Kolla, and J. Eckert, "Additive manufacturing processes: Selective laser melting, electron beam melting and binder jetting—Selection guidelines," *materials*, vol. 10, no. 6, p. 672, 2017.

[9] A. Hadadzadeh, B. S. Amirkhiz, B. Langelier, J. Li, and M. Mohammadi, "Microstructural consistency in the additive manufactured metallic materials: A study on the laser powder bed fusion of AlSi10Mg," *Addit Manuf*, vol. 46, p. 102166, Oct. 2021, doi: 10.1016/J.ADDMA.2021.102166.

[10] H. Hyer *et al.*, “Understanding the laser powder bed fusion of AlSi10Mg alloy,” *Metallography, Microstructure, and Analysis*, vol. 9, no. 4, pp. 484–502, 2020.

[11] K. Kempen, L. Thijs, J. van Humbeeck, and J.-P. Kruth, “Mechanical properties of AlSi10Mg produced by selective laser melting,” *Phys Procedia*, vol. 39, pp. 439–446, 2012.

[12] S. I. Shakil, A. Hadadzadeh, B. Shalchi Amirkhiz, H. Pirgazi, M. Mohammadi, and M. Haghshenas, “Additive manufactured versus cast AlSi10Mg alloy: Microstructure and micromechanics,” *Results in Materials*, vol. 10, p. 100178, Jun. 2021, doi: 10.1016/J.RINMA.2021.100178.

[13] Y. Kok *et al.*, “Anisotropy and heterogeneity of microstructure and mechanical properties in metal additive manufacturing: A critical review,” *Mater Des*, vol. 139, pp. 565–586, 2018.

[14] M. J. Paul *et al.*, “Fracture resistance of AlSi10Mg fabricated by laser powder bed fusion,” *Acta Mater*, vol. 211, p. 116869, Jun. 2021, doi: 10.1016/J.ACTAMAT.2021.116869.

[15] S. AlRedha *et al.*, “Effect of build orientation on fracture behaviour of AlSi10Mg produced by selective laser melting,” *Rapid Prototyp J*, 2020.

[16] L. Zhao, J. G. Santos Macías, T. Douillard, Z. Li, and A. Simar, “Unveiling damage sites and fracture path in laser powder bed fusion AlSi10Mg: Comparison between horizontal and vertical loading directions,” *Materials Science and Engineering: A*, vol. 807, p. 140845, Mar. 2021, doi: 10.1016/J.MSEA.2021.140845.

[17] D. Balageas, C.-P. Fritzen, and A. Güemes, *Structural health monitoring*, vol. 90. John Wiley & Sons, 2010.

[18] F. Bjørheim, S. C. Siriwardane, and D. Pavlou, “A review of fatigue damage detection and measurement techniques,” *Int J Fatigue*, vol. 154, p. 106556, Jan. 2022, doi: 10.1016/J.IJFATIGUE.2021.106556.

[19] A. Modir and I. Tansel, “Wave Propagation and Structural Health Monitoring Application on Parts Fabricated by Additive Manufacturing,” *Automation*, vol. 2, no. 3, pp. 173–186, 2021.

[20] S. Dharmadhikari and A. Basak, “Evaluation of Early Fatigue Damage Detection in Additively Manufactured AlSi10Mg,” in *2021 International Solid Freeform Fabrication Symposium*, 2021.

[21] W. M. Murray and W. R. Miller, *The bonded electrical resistance strain gage: an introduction*. Oxford university press, 1992.

[22] R. L. Hannah and S. E. Reed, *Strain gage users’ handbook*. Springer Science & Business Media, 1992.

[23] A. Perbawa, E. Gramajo, T. Finkbeiner, and J. C. Santamarina, “Rock Triaxial Tests: Global Deformation vs Local Strain Measurements—Implications,” *Rock Mech Rock Eng*, vol. 54, no. 7, pp. 3527–3540, 2021.

[24] J. Lee, “Application of strain gauge method for investigating influence of ship shaft movement by hydrodynamic propeller forces on shaft alignment,” *Measurement*, vol. 121, pp. 261–275, 2018.

[25] S. Rawal, J. Brantley, and N. Karabudak, “Additive manufacturing of Ti-6Al-4V alloy components for spacecraft applications,” in *2013 6th international conference on recent advances in space technologies (RAST)*, 2013, pp. 5–11.

[26] M. Rumsey *et al.*, “Experimental results of structural health monitoring of wind turbine blades,” in *46th AIAA aerospace sciences meeting and exhibit*, 2008, p. 1348.

[27] M. E. Tuttle and H. F. Brinson, “Resistance-foil strain-gage technology as applied to composite materials,” *Exp Mech*, vol. 24, no. 1, pp. 54–65, 1984.

[28] B. L. Ellis and L. M. Smith, “Modeling and experimental testing of strain gauges in operational and failure modes,” *IEEE Trans Instrum Meas*, vol. 58, no. 7, pp. 2222–2227, 2009.

[29] J. dos Reis, C. Oliveira Costa, and J. Sá da Costa, “Strain gauges debonding fault detection for structural health monitoring,” *Struct Control Health Monit*, vol. 25, no. 12, p. e2264, 2018.

[30] “ASM Material Datasheet.” https://asm.matweb.com/search/SpecificMaterial.asp?bassnum=ma6061t6 (accessed Mar. 01, 2023).

[31] ASTM E466-07, “Standard practice for conducting force controlled constant amplitude axial fatigue tests of metallic materials,” *ASTM International*, 2007.

[32] S. Dharmadhikari and A. Basak, “Evaluation of Early Fatigue Damage Detection in Additively Manufactured AlSi10Mg,” in *2021 International Solid Freeform Fabrication Symposium*, 2021.

[33] “MCA-1 M-Prep Conditioner A,” *Micro Measurements: A VPG Brand*.

[34] “MathWorks Help Center: Butter,” 2023. https://www.mathworks.com/help/signal/ref/butter.html (accessed Mar. 02, 2023).

[35] R. G. Budynas and J. K. Nisbett, *Shigley’s Mechanical Engineering Design*, 11th ed. McGraw Hill Education, 2020.

[36] T. R. Chandrupatla and A. D. Belegundu, *Introduction to Finite Elements in Engineering*, 4th ed. Pearson, 2012.

[37] *Abaqus: Analysis User’s Manual*, 6.12., vol. V. SIMULIA, 2012.

[38] Y. Zhang *et al.*, “Serration and noise behaviors in materials,” *Progress in Materials Science*, vol. 90. 2017. doi: 10.1016/j.pmatsci.2017.06.004.

ACADEMIC VITA

CALEB FRONK

Education

Pennsylvania State University, **Schreyer Honors College**, University Park, PA 2019-2023
Bachelor of Science, Mechanical Engineering May 2023

Excellence Awards: Mechanical Engineering Shuman Scholarship, College of Engineering AMETEK Foundation Scholarship, Evan Pugh Scholar Award, Aero Pioneers Scholarship

Research Experience

Basak Laboratory - Penn State University, PA August 2021-Present

- Utilize strain gauges to correlate and study local and global tensile deformation of additively manufactured AlSi10Mg samples produced via laser powder bed fusion.
- Presented at TMS (minerals, metals, materials society) Conference 2023. Earned 1st place in Undergraduate Student Poster Competition for Light Metals Division

Work Experience

Pratt and Whitney - East Harford, CT Summer 2022
Job Title: HCF Core Structures Engineering Intern

- Analyzed and reduced airfoil vibration data for validation of high-cycle fatigue requirements
- Integrated and proposed a new metric for assessing strain gauge signal quality; pitched idea to subject matter experts; improved automated data identification process by 50%.
- Researched output file reduction methods in signal processing software

Penn State Formula Racing Team - University Park, PA August 2021 - Present

- Design and manufacture carbon fiber chassis components for student made F1 Racecar
- Research and organize transition to full monocoque for the 2023 competition; appointed lead designer of composite layup; focused on incorporating aramid core into layup for first time
- Conduct and facilitate mechanical tests of composite sandwich panels. Led processing of mechanical test data. Completed chassis rules spreadsheet (SES) to ensure frame design safety.

Mid-Atlantic Regional Maintenance Center - Naval Station Norfolk, VA Summer 2021
Job Title: Mechanical Engineering Intern

- Assessed, repaired, and tested systems and equipment on over 20 U.S. Naval Vessels
- Primarily assessed various auxiliary equipment: heat exchangers, valves, main condensers, reverse osmosis units, fire pumps, lube oil purifiers, fuel oil pumps, and main distiller units
- Shadowed team-assessing condition of main reduction gears on a guided missile destroyer
- Aided in maintenance of combat systems equipment such as Phalanx CIWS and MK-45 5" Gun
- Maintained active Department of Defense Secret Security Clearance

Leadership Experience

Eagle Scout Project - Steelton, PA October 2018- June 2019

- Completed project for "Stop the Violence Ministry", which aids victims of domestic abuse
- Led, organized, and directed total of 30 volunteers (children and adults)
- Fundraised total of $4,000, covering entire project's expenses and donating to beneficiary
- Restored and repaired outdoor porch, siding, fencing, etc. as part of complete shelter overhaul